This article has been accepted for publication in IEEE Transactions on Antennas and Propagation. This is the author's version which has not been fully edited and content may change prior to final publication. Citation information: DOI 10.1109/TAP.2023.3240085

Beamforming Phased-array-fed Lenses with >0.5λ–spaced Elements

Wei Wang, *Student Member, IEEE,* Nicholas Estes, *Student Member, IEEE,* Nicolas Garcia, *Student Member, IEEE,* Matthew Roddy, *Student Member, IEEE,* Andrew Bolstad, *Senior Member, IEEE* Jonathan Chisum, *Senior Member, IEEE*

***Abstract*—We propose a phased-array-fed lens (PAFL) antenna which is capable of beamforming like a phased array but with array elements spaced beyond 0.5λ. The PAFL produces high quality scanned beams using only five active feeds. This architecture represents a dramatic cost and power savings over conventional phased arrays while providing many of the features. We present an optimal beamforming method to achieve maximum gain at any angle using a subset of feeds and a multi-objective optimizer using particle swarm optimization for more granular pattern control. The method is applied to several simulated state-of-the-art lens antennas with good performance confirming the generality of the method. The theory is demonstrated with a prototype PAFL comprising a 4" aperture GRIN lens antenna, an 8-element 0.725λ–spaced linear patch array operating at 29 GHz, and a commercial Ka-band SATCOM beamformer IC. The prototype achieves maximum gain at all angles and improves scan loss by 4 dB at $\pm 50°$.**

***Index Terms*—GRIN lenses, beamforming, phased-array, electromagnetic metamaterials, lens antennas, millimeter-wave**

I. Introduction

RECENT advances in millimeter wave (MMW) communications have ushered in a new era of high speed wireless data proliferation. Emerging 5G mobile wireless networks and low earth orbit (LEO) satellite-enabled space internet will make extensive use of the MMW bands. High performance beamforming antennas are essential to the realization of these services and are anticipated to be deployed on a massive scale: it is estimated that by 2030 over 2 million base-stations (BS) and small cells (SC) will be deployed in 5G-MMW infrastructure and by 2040 up to 19 million LEO SATCOM terminals will be installed with end-users (e.g., homes).

The current preferred antenna system for these applications is the phased array antenna (PAA) [1] as depicted in Fig. 1(a). Modern PAAs demonstrate exceptional beamforming performance and consistently achieve low scan loss, wide field-of-view (FoV), multi-beam capabilities, and beam-shaping [2]–[9]. However, in order to realize this degree of reconfigurability, PAA elements must maintain $\lambda/2$ spacing. High-gain PAAs thus require a large number (P, ranging from 100's to 1000's) of elements and corresponding beamformer ICs, making PAA solutions costly and power-inefficient. Given the broad scope of anticipated deployment, high performance PAAs are not always a practical solution.

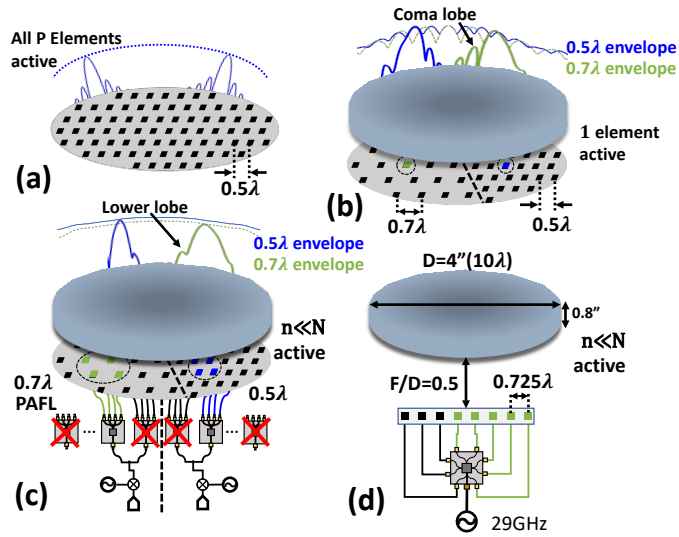

Fig. 1. (a) A phased-array with 0.5λ–spaced feeds. All P feeds are active for all beam angles. (b) A switch-beam lens antenna uses a single feed for each beam angle and is not confined to 0.5λ spacing but cannot scan to arbitrary angles or shape the beam. (c) The proposed phased-array-fed lens antenna combines a widely spaced (0.7λ) phased-array feed with N elements ($N < P$) and a lens to reproduce the capabilities of a phased array using a small collection of n feeds ($n << N < P$). (d) The prototype PAFL employing 4" (101.6 mm) gradient-index (GRIN) lens antenna with focal length F = 2" and 8-element 29 GHz linear patch array (0.725λ–spaced) driven by a commercial Ka-band SATCOM transmit beamformer IC.

In an effort to reduce cost and power, various alternative PAA configurations have been proposed. For example, 'thinned' phased array systems selectively turn off elements based on optimization algorithms and thus achieve lower power consumption while retaining a critically sampled array [10]–[12]. Similarly, 'sparse' phased array systems reduce the total element count using optimized element locations that exceed the critical sampling threshold, further reducing cost [12]–[17]. However, these techniques are unsuitable for aggressive beamforming due to their relatively narrow FoV, propensity for grating lobes [12], [18], and inability to explicitly control the beam shape.

An alternative approach to PAA beamscanning is the

Manuscript received November 22, 2021; revised December 10, 2022. This work was supported in part by the National Science Foundation under award CNS-1439682-011 (BWAC IUCRC) and the Department of the Navy, Office of Naval Research under contract N00014-20-C-1067. Distribution A: Approved for public release: Distribution Unlimited. *Corresponding author: Jonathan D. Chisum.*

Wei Wang and Nicholas Estes contributed equally as lead authors.

Wei Wang, Nicholas Estes, Nicolas Garcia, and Jonathan Chisum are with the Department of Electrical Engineering, University of Notre Dame, Notre Dame, IN, 46556 USA (e-mail: wwang23@nd.edu; nestes@nd.edu; abolstad@iastate.edu; jchisum@nd.edu). Matthew Roddy was with the Department of Electrical Engineering, University of Notre Dame at the time of the work and is now with Cornell University, Ithaca, NY, 14850 USA. Andrew Bolstad is with the Department of Electrical and Computer Engineering, Iowa State University, Ames, IA, 50011, USA.

© 2023 IEEE. Personal use is permitted, but republication/redistribution requires IEEE permission. See https://www.ieee.org/publications/rights/index.html for more information.
Authorized licensed use limited to: UNIVERSITY NOTRE DAME. Downloaded on February 14,2023 at 18:29:53 UTC from IEEE Xplore. Restrictions apply.

This article has been accepted for publication in IEEE Transactions on Antennas and Propagation. This is the author's version which has not been fully edited and content may change prior to final publication. Citation information: DOI 10.1109/TAP.2023.3240085

switched-beam gradient index (GRIN) lens antenna as shown in Fig. 1(b). Modern MMW GRIN lenses demonstrate high aperture efficiency and extremely wide bandwidths [19]–[33]. GRIN lenses can also achieve high quality beam-scanning over a wide FoV by utilizing Luneburg-type lenses [22]–[26], [33], [34] or compound lens systems [35], [36]. In this configuration, each feed element beneath the lens generates a beam at a particular angle and scanning is achieved by activating one element at a time. Given the passive nature of the lens and the near-absence of active electronics, this system is highly power efficient. However, switched-beam systems are constrained by the element sampling and thus cannot scan to arbitrary angle or apply beam-shaping. The latter is of particular concern for far-scanned beams where beam qualities (i.e., gain, sidelobe level, coma lobe) are most degraded.

The beamforming performance of switched beam systems can be improved by feeding the focusing element with a PAA—this approach has been demonstrated with both lens systems and reflectors (for which the low-power switched-beam method is also viable) [37]–[47]. In the latter context, the phased-array-fed-reflector (PAFR) technique is employed to achieve optimal illumination but is not typically used for wide-angle scanning. Indeed, PAFRs demonstrate a high degree of flexibility but are constrained by the limited FoV intrinsic to high-gain reflector systems [48]–[50] and suffer from feed blockage.

Phased array fed lens (PAFL) designs are potentially more appealing for wide-FoV applications and have no feed blockage, but to date the concept has not been fully explored. In [41], a feed array and lens were co-designed using FEM and GO techniques, but the lens was not fed at the approximate focal plane, leading to a large number of simultaneously active antennas. In addition, the design methodology optimized for directivity only, ignoring side lobe level (SLL). In [42], amplitude-only beamforming strategies are explored in simulation to fill the low-gain nulls between available beams. In [43], a beamforming array is employed behind a metasurface-based lens in order to reduce the antenna system depth by feeding forward of the focal point. This necessarily requires a larger number of active feed antennas, and the investigation considers only gain maximization using phase control. In [44], an array-fed lens antenna system is employed for beam-shaping, but only considers the case in which a wide beam is desired, which allows for amplitude-only beamforming assuming equal feed phase. In [45], an optimization for feed weights employing target beam shapes is used to improve beamscan performance in a dielectric lens antenna. In [46], [47], a theoretical lens antenna array model is derived assuming lenses with large F/D and it shows reduced signal processing complexity compared with arrays. In [51], a beam-switching array is designed with a Rotman lens and realizes fixed beam scanning up to $\pm 30°$.

In this work we propose a PAFL antenna which combines N widely spaced ($> 0.5\lambda$) phased-array feed elements to further reduce power, cost, and complexity as shown in Fig. 1(c). As we will show, the PAFL has a well-behaved scan envelope (with reduced scan loss relative to a single lens antenna and no nulls between beams), controlled sidelobes, low-coma lobe, and even multi-beam operation. Due to the feed array sparsity, a PAFL requires fewer total feed array elements than a corresponding PAA ($N < P$) and can even generate a given beam using a smaller number, $n << N$, of the available feed elements. For example, our 0.725λ–spaced, 8-element prototype [see Fig. 1(d)] discussed in Section IV uses $2.1\times$ fewer feeds than a critically sampled PAA and requires as few as 4–6 active feeds to produce high quality beams. The PAFL offers a continuous trade-space between a PAA (P active feeds) and a switch beam antenna (1 active feed). That is, $1 < n << N < P$, which represents a significant cost savings and potentially orders of magnitude lower power dissipation relative to a PAA while being able to produce significantly higher quality beams than a switch-beam lens antenna and at arbitrary angles. The flexibility, performance, and potential for cost and power savings of the PAFL offer a compelling solution for the massive deployment of high-gain MMW beamscanning antennas that are required for current and future wireless communications systems.

One of the key contributions of this work in Section II is a proposed system model and theoretical framework for PAFL with optimal feed weights as well as a multi-objective PSO method for finding feed weights. We develop an optimal solution which only requires complex far-fields[1] at the desired angle. This is in contrast to the conjugate field matching approach used in [37]–[40] which requires knowledge of the fields in the focal plane (often a difficult quantity to measure), therefore this method is simpler to implement. Another key contribution of this work in Section III is a robust exploration of the tradeoffs of feed spacing and the conclusion that spacing on the order of 0.7λ is often acceptable. In Section IV we demonstrate high quality beamscanning with the proposed method, achieving an improved scan loss exponent. Finally, in Section V we show that the PAFL can realize many of the most important capabilities of a PAA and we demonstrate the method is general by applying it to several state-of-the-art lenses from the literature. While the PAFL approach can generally improve the performance of a switch-beam lens antenna system, beamscan performance is fundamentally limited by the FoV of the basis beams—therefore the lens should be designed for wide-FoV operation. Further, since $n << P$, the effective isotropic radiated power (EIRP) of a PAFL system will be lower than an equivalently sized PAA. This is discussed further in Section VI.

II. Beamforming Theory

In this section we describe the system model and derive the optimal complex feed weights to achieve maximum gain at arbitrary scan angles across the FoV. We also introduce a multiobjective optimization method employing particle swarm optimization (PSO) to find the globally optimal weights for satisfying multiple FoMs.

[1] In Section III the reader will note that we use a near-field antenna range to capture the far-field pattern. This is fundamentally different from the conjugate field mapping approach because the near-field antenna range only scans *outside* the physical envelope of the integrated feed-array/lens system.

© 2023 IEEE. Personal use is permitted, but republication/redistribution requires IEEE permission. See https://www.ieee.org/publications/rights/index.html for more information.
Authorized licensed use limited to: UNIVERSITY NOTRE DAME. Downloaded on February 14,2023 at 18:29:53 UTC from IEEE Xplore. Restrictions apply.

This article has been accepted for publication in IEEE Transactions on Antennas and Propagation. This is the author's version which has not been fully edited and content may change prior to final publication. Citation information: DOI 10.1109/TAP.2023.3240085

A. Problem Setup, General Formulation

In order to motivate widely-spaced feed elements, consider the idealized PAFL system shown in Fig. 2(a) in which the n and $n+1$ feed elements produce far-field electric fields $E_{\theta,n}(\theta,\phi)$,$E_{\phi,n}(\theta,\phi)$ and $E_{\theta,n+1}(\theta,\phi)$,$E_{\phi,n+1}(\theta,\phi)$, respectively. The corresponding beam angles are separated by $\Delta\theta$ equal to the angular spacing of the feeds (as in an idealized Luneburg lens) and have a crossover gain G_x that is below the feed beam peaks (G_b). In this paper we refer to the beam produced by a single feed element as a *basis beam*. The n and $n+1$ feed elements are driven by complex weights s_n and s_{n+1}, respectively and are separated by an arc length $R\Delta\theta$. If the lens is assumed to produce an idealized uniform aperture field distribution at all feed angles the resulting beams are sinc functions versus angle.

Assuming any two feed locations are fixed there is a region with lower gain between each basis beam (referred to as the "null"). To 'fill the null' all N beams can be optimally combined to produce the highest gain at the angle exactly between the two basis beams (using the gain solution of Appendix A). This synthesized beam can in fact have higher gain at the null than each basis has individually, and the ratio of the gain of this synthesized beam to G_b is denoted as ΔG. As the spatial (or angular) separation between feed n and $n+1$ increases G_x reduces and filling this null becomes more difficult (Fig. 2(b)). The mapping from crossover to spacing is shown explicitly in Fig. 2(c) for a variety of assumed aperture efficiencies (marked as η_{ap}) ranging from 0.6 to 0.8. For feed spacing out to approximately 0.7λ the gain between two beams can be approximately equal to the gain of the basis beams (at their corresponding angles). If the feeds are closer (e.g., 0.5λ), ΔG (in dB) actually becomes positive. This simplified analysis justifies the feed approach proposed in this work.

Fig. 2(c) also summarizes the various simulations and measurements included in the remainder of this work. The theoretical Luneburg lens simulations (solid traces) with different η_{ap} (and correspondingly, different beamwidths) are representative of a wide range of practical antennas and demonstrate that feed elements could be spaced between 0.6–0.8λ with no significant drop in gain ($\Delta G \geq 0$ dB) across the FoV. Between these theoretical curves, several practically-realized feed/lens systems are included. The purple circle markers show the measured gain improvement using the standard gain horn feed-antennas over a wide range of feed spacing from 0.5–1.0λ, as discussed in Section III. These results indicate that gain begins to drop for feed spacing beyond 0.8λ. Green triangle markers show simulated gain improvement using an open-ended waveguide-fed lens, and confirm a feed spacing of 0.8λ—this investigation is discussed in Section V. These preliminary investigations indicate that a 0.7λ–0.8λ feed spacing range can maintain gain across the FoV. Therefore, the prototype PAFL system discussed in Section IV of this work is a 0.725λ–spaced feed array (indicated with magenta triangle markers).

One of the objectives of this work is to establish a method for computing optimal feed weights $\boldsymbol{s}$ for a desired objective (e.g., maximum gain at an arbitrary angle, including between basis beams) based upon measured (or simulated) complex

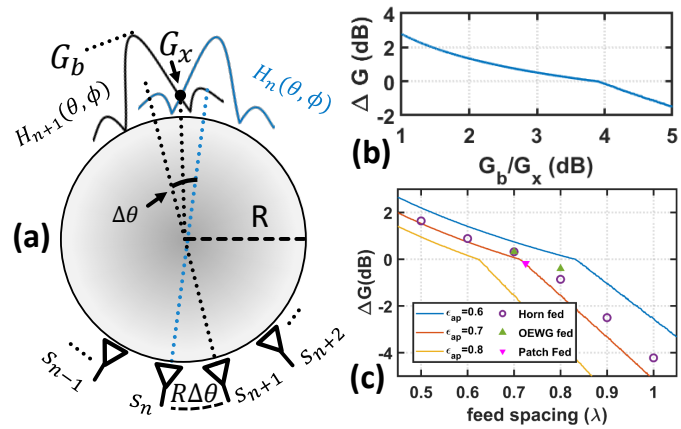

Fig. 2. (a) Model of a PAFL system. assuming an idealized sinc-pattern lens with no scan loss. (b) For this model, beamforming can increase gain relative to the basis beams as long as the crossover between adjacent beams is less than about 3.8 dB. As such it represents a cutoff for high-performance operation. (c) Beamformed gain improvement over feed spacing for multiple aperture efficiencies (η_{ap}). Higher aperture efficiency lenses benefit less from beamforming. For the lens employed in this work, 0.7λ corresponds approximately to a ΔG of 0 dB. Vertical dashed lines indicate the feed spacings investigated further and shown in Fig. 4.

fields (or radiation patterns) from a realized system. Since each feed produces a single basis beam which is scaled by the complex weight of each feed $\boldsymbol{s}$ and the total field is the superposition of all feeds, the resulting electric field in the far-field can be expressed as a vector of complex feed weights multiplied by a lens system matrix, $\boldsymbol{H}$,

$$\boldsymbol{e} = \boldsymbol{H}\boldsymbol{s}, \tag{1}$$

where $\boldsymbol{H} \in \mathbb{C}$ is an $M \times N$ matrix consisting of the electric field response at M angles (θ,ϕ) in the far-field due to a unit-excitation at each of the N feed elements. $\theta \in [\frac{-\pi}{2}, \frac{\pi}{2}], \phi \in [-\pi,\pi]$. $M/2$ of the rows represent E_θ and the remaining $M/2$ represent E_ϕ. Each column represents the nth basis beam. The $N\times 1$ $\boldsymbol{s} \in \mathbb{C}$ are phasors representing normalized driving point voltages such that s_n^2 is equivalent to input power at the nth feed. We use the convention that boldface capital letters denote matrices and boldface lower-case letters denote vectors. Below is an example of this matrix, where the first index refers to far-field angle θ and the second to ϕ and the subscripts indicate field polarization and feed index:

$$\boldsymbol{H} = \begin{bmatrix} E_{\theta,1}(-\pi,0) & \dots & E_{\theta,N}(-\pi,0) \\ \vdots & \ddots & \vdots \\ E_{\theta,1}(\theta_0,\phi_0) & \dots & E_{\theta,N}(\theta_0,\phi_0) \\ \vdots & \ddots & \vdots \\ E_{\theta,1}(\pi,2\pi) & \dots & E_{\theta,N}(\pi,2\pi) \\ E_{\phi,1}(-\pi,0) & \dots & E_{\phi,N}(-\pi,0) \\ \vdots & \ddots & \vdots \\ E_{\phi,1}(\theta_0,\phi_0) & \dots & E_{\phi,N}(\theta_0,\phi_0) \\ \vdots & \ddots & \vdots \\ E_{\phi,1}(\pi,2\pi) & \dots & E_{\phi,N}(\pi,2\pi) \end{bmatrix}. \tag{2}$$

© 2023 IEEE. Personal use is permitted, but republication/redistribution requires IEEE permission. See https://www.ieee.org/publications/rights/index.html for more information.
Authorized licensed use limited to: UNIVERSITY NOTRE DAME. Downloaded on February 14,2023 at 18:29:53 UTC from IEEE Xplore. Restrictions apply.

This article has been accepted for publication in IEEE Transactions on Antennas and Propagation. This is the author's version which has not been fully edited and content may change prior to final publication. Citation information: DOI 10.1109/TAP.2023.3240085

The $M \times 1$ vector $\boldsymbol{e} \in \mathbb{C}$ is the resulting total electric field due to a particular array excitation. The matrix in (2) is referred to as the "H matrix". In some cases we will select $M < N$ columns of the H matrix (feeds) to form an H submatrix. Such submatrices will also be referred to as H matrices or $\boldsymbol{H}$ unless the distinction is relevant. We present two algorithms below to determine the appropriate feed weights $\boldsymbol{s}$ for a high-quality beam at a given steering angle: a rigorously accurate "max gain" algorithm generated from constrained optimization theory and a global solver implemented using particle swarm optimization (PSO).

It may be shown (see Appendix A), that the maximum possible gain is achieved at angle (θ_0, ϕ_0) when:

$$\boldsymbol{s} = \boldsymbol{h}_0^*, \tag{3}$$

where $\boldsymbol{h}_0$ is the row vector of $\boldsymbol{H}$ corresponding to the (θ_0, ϕ_0) steering angle and $(\cdot)^*$ is the conjugate transpose operator. Moreover, when removing columns from $\boldsymbol{H}$ (reducing the number of simultaneously active feeds), it may be shown that the feeds corresponding to the smallest magnitude elements of $\boldsymbol{h}_0$ should be removed first (see Appendix A). For other figures of merit this selection criterion is no longer rigorously true but remains a useful heuristic.

The maximum gain solution is closed-form and essentially instantaneous to compute. However, it possesses some drawbacks, namely:

1) It only optimizes gain and cannot address, e.g., sidelobe levels directly.
2) Although the gain in the direction of the steering angle is guaranteed to be the maximum possible for the set of feeds chosen, the steering angle is *not guaranteed to be the angle at which the radiation pattern is maximized* (that is, the gain may be higher at other angles).

Alternatively, a FoM can be defined to describe the desired beam(s) and a global optimizer can be used to solve for the beam weights that produce the highest FoM. We investigate such a global solver employing PSO in the next section.

B. PSO Solver

To define a useful FoM, we first consider the desirable aspects of a beam (see Fig. 3(b)):

1) high gain at steering angle $G(\theta_0)$,
2) low sidelobe level (SLL),
3) angle of maximum gain corresponds to desired beam angle (θ_0), and
4) low main-beam width $(\Delta\theta)$.

Although in practice there may be some correlation between these characteristics, it is convenient to track each of these characteristics independently. A total FoM may be defined as

$$FoM = \frac{\sum_i w_i f_i(\boldsymbol{Hs})}{\sum_i w_i}, \tag{4}$$

where the $f_i(\boldsymbol{Hs})$ denotes a functional assigning a scalar 'score' to a beam-characteristic-specific FoM and the w_i are scalar weights to assign relative importance. We choose here to define our f_i using integrated sigmoids. Sigmoid cost functions

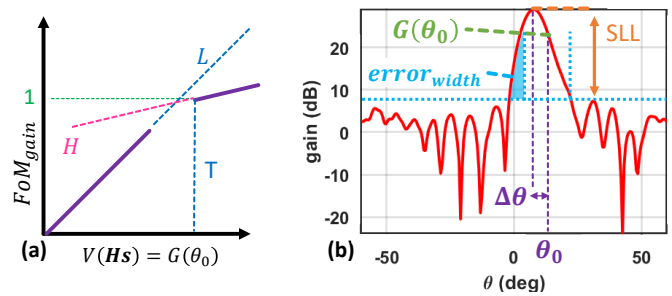

Fig. 3. a) Example integrated sigmoid component FoM for gain, which exhibits a constant slope (L) up until around the target gain (T), at which point the slope transitions to another constant slope (H), with transition sharpness K ("knee"). b) The full FoM considers steering angle accuracy, gain at the steering angle ($G(\theta_0)$, SLL, beam angle ($\Delta\theta$), and main beam width $error_{\text{width}}$.

are common in optimization frameworks and sigmoids have also recently been employed specifically in particle swarm optimization approaches to dynamically alter the acceleration coefficients [52]–[54]. Since sigmoids are a class of function that are continuous, monotonic, differentiable, and asymptotically *constant*, then integrated sigmoids are continuous, monotonic, and differentiable, and asymptotically *linear*:

$$f_i(\boldsymbol{Hs}) = \frac{H-L}{K}\left[log(Ke^{T-V(\boldsymbol{Hs})}+1)\right] + L(T-V) + 1, \tag{5}$$

where $V(\cdot)$ is a functional that maps $\boldsymbol{Hs}$ to a scalar beam characteristic such as Gain and T is the target value of $V(\boldsymbol{Hs})$. L denotes the asymptotic slope when $V(\boldsymbol{Hs}) < T$, H denotes the asymptotic slope when $V(\boldsymbol{Hs}) > T$, and K is a parameter controlling the transition sharpness at T. In general, $V(\boldsymbol{Hs}) \geq T$ should represent a good component FoM score. Fig. 3(a) shows an example of an integrated-sigmoid FoM component curve. The major benefits of the integrated sigmoid function are:

- Since the sigmoid is differentiable, gradient-based approaches may be employed if necessary.
- The asymptotic slopes may be tuned such that the importance of improving a component FoM score diminishes once a desired target T has been hit – however, there is still an incentive to improve upon this value if possible

$V(\boldsymbol{Hs})$ and T are defined for each component FoM. With reference to the four desirable quantities of beams above (and Fig. 3(b)):

1) High gain: $V(\boldsymbol{Hs})$ and T are defined logarithmically—T is at or above the basis gain.
2) Low SLL: $V(\boldsymbol{Hs})$ is the difference in logarithms between the global gain peak and the highest sidelobe peak. T is generally set from -10 to -15 dB.
3) Steering angle: $V(\boldsymbol{Hs})$ is the angle of the beam pattern maximum. T is the desired beam angle.
4) Low beam width: $V(\boldsymbol{Hs})$ is the integral of the logarithmic gain above a threshold (shown graphically as the SLL threshold) in an angular region excluding the desired beam width. T is zero. Fig. 3b shows an example region of integration ($error_{\text{width}}$).

© 2023 IEEE. Personal use is permitted, but republication/redistribution requires IEEE permission. See https://www.ieee.org/publications/rights/index.html for more information.
Authorized licensed use limited to: UNIVERSITY NOTRE DAME. Downloaded on February 14,2023 at 18:29:53 UTC from IEEE Xplore. Restrictions apply.

This article has been accepted for publication in IEEE Transactions on Antennas and Propagation. This is the author's version which has not been fully edited and content may change prior to final publication. Citation information: DOI 10.1109/TAP.2023.3240085

These FoMs will be referred to as f_{gain}, f_{SLL}, f_{angle}, and f_{BW} for notational consistency with (5). Their corresponding weights are referred to as w_{gain}, w_{SLL}, w_{angle}, and w_{BW}. f_{gain} was assigned an H of 0.2 to allow for unlimited gain improvement and all other f_i had $H = 0$.

For all optimized beam weights, the MATLAB "particleswarm" function (from the Global Optimizer Toolbox) was used, although many particle swarm implementations exist. Convergence is aided by seeding half of the particles within a 2N-dimensional sphere centered at the solution of the max gain solver, which reduces the number of iterations by a factor of 2. More sophisticated strategies for improving optimizer efficiency may be necessary for tractable lens-array co-design, but were not required for this work and will not be discussed further. In the following two sections we will validate the above theory and demonstrate it with a prototype PAFL and commercially available Ka-band SATCOM transmit beamformer IC.

III. Validation

A. Null-Filling, Maximum Gain

In this section the theoretical results from Section II will be validated using a 4"-diameter (101.6 mm) planar GRIN lens (described in [19], [30]) and fed with 10 dBi standard gain horn antennas. Fed in such a way the lens has broadside aperture efficiency above 60% over the WR-28 band (26.5 to 40 GHz). In order to confirm the gain-improvement (ΔG) versus feed spacing from the simplified analysis (Fig. 2c) the feed horn was placed across the bottom of the lens (in the focal plane) in steps of 0.1λ. At each location the complex far-field basis beams were recorded using an NSI-MI near field scanner with an angular coverage up to $60°$ from broadside. A full edge-to-edge set of basis beams was created by assuming symmetry across the lens center. While a 0.1λ feed spacing is not physically realizable, the tight spacing on measured beams allowed us to better investigate the effect of array spacing on beam quality (specifically $d = 0.5\,\lambda$, $d = 0.7\,\lambda$, and $d = \lambda$, as shown by the columns of Fig. 4 and inspired by the results of Fig. 2(c)). The measured basis beams are shown in Fig. 4(a)-(c). This system has high quality near-broadside basis beams, exhibiting -20 dB SLL. Beam quality noticeably degrades over scan with farther-out beams exhibiting reduced gain, larger beamwidth and reduced SLL. Throughout this manuscript gain reduction versus scan angle will be characterised with an empirical scan-loss exponent where gain reduces as $\cos^{n_s}(\theta)$. For example, the scan-loss exponent of the basis beams is $n_s = 5.0$.

Fig. 4(d-l) shows the null-filling results for each array spacing. Using (3), we synthesize maximum-gain beams only at the nulls from $\theta = 0°$ to the edge beams, shown in Fig. 4(d)-(f). Even though we are forming beams at the 'worst-case' locations, the beams synthesized by the 0.5λ and 0.7λ arrays show better gain and lower scan loss than the bases. Specifically, the $cos^5(\theta)$ scan loss of the bases go to $\cos^{3.2}(\theta)$ for the 0.5λ array and $\cos^{3.6}(\theta)$ for the 0.7λ array. Note the poor quality and low gain of the 1λ array beams, as expected from Fig. 2(c), because it greatly exceeds the approximately 0.8λ spacing limit.

To better visualize beam quality and achievable gain between basis beams, we synthesize only near-broadside beams in Fig. 4(g-l), that is, between the broadside beam at $\theta = 0$ and the next closest basis beam. For the 0.5λ and 0.7λ arrays (Fig. 4(g)(h))), the synthesized beams attain higher gain than their respective basis beams while retaining extremely low sidelobe level ($SLL < -20\,dB$). For the 1λ array (Fig. 4(f)), achievable gain at the null angle is in fact greater than that achievable by any single basis at that angle, but the null beams do not have gain commensurate with the bases and exhibit poor quality. Fig. 4(j)-(l) are zooms of the peaks of Fig. 4(g)-(i), respectively. The 0.5λ synthesized beams have an additional 1.46 dB of gain compared to the basis beams, and the 0.7λ synthesized beams can fill the null with only marginal improvement in gain at the broadside basis (0.16 dB). For the 1λ array (Fig. 4(k)), the beams synthesized exhibit either severe degradation within the beam null or exhibit a maximum gain that does not coincide with the steering angle.

Fig. 5(a)-(d) shows the peak gain achievable at any given steering angle from $0° - 45°$. For comparison, the maximum gain at each steering angle due to excitation of a single basis beam is also shown. For all three spacings, the basis beam envelopes are lower than synthesized beam envelopes with ripples representing nulls. Fig. 5(a) shows the improved scan loss of $\cos^{3.2}\theta$ for 0.5λ spacing and Fig. 5(b) shows the improved scan loss of $\cos^{3.6}\theta$ for 0.7λ spacing. For the 1λ spacing of Fig. 5(c), the synthesized gain envelope follows the basis nulls for low beamscan, but can eventually fill the nulls for large scan angle due to the relatively high crossover of the far basis beams. Fig. 5(d) directly compares the gain envelope for the three feed spacings, indicating a tradeoff between power consumption and maximum gain.

B. Multiobjective Beamforming

Although the previous results were all achieved using (3), PSO provides far greater control over the beam patterns. If w_{gain} dominates or the beams are near broadside, the PSO results agree almost perfectly with the maximum gain solution as seen in Fig. 6(a). However, especially for beamscan, if either f_{SLL} or f_{BW} are relatively highly weighted, the synthesized PSO and 'maximum gain' beams will differ, as shown in Fig 6(b). The reference beam is from Fig. 4(e) for an 18° target with a target 3-dB beamwidth of 9.6° and SLL of 20 dB. By assigning larger weights for SLL and beamwidth, the PSO-synthesized beam achieves a 3-dB beamwidth of only 8.3° and a SLL of 23 dB with 0.7 dB gain reduction (relative to the maximum gain solution). Overall, the result shows the feasibility of PSO in practical beamforming synthesis.

IV. Beamforming Measurement and Results

Now that the method has been demonstrated with measured data (albeit collected from a single scanned feed element), in this section we validate the method using a practical phased-array feed. Figure 7(a) shows the prototype measurement setup where the same 4" GRIN lens is fed by an 8-element patch array which is driven by a beamformer IC. Fig 7(b)(c) show the side view and zoom figure of the measurement setup.

© 2023 IEEE. Personal use is permitted, but republication/redistribution requires IEEE permission. See https://www.ieee.org/publications/rights/index.html for more information.
Authorized licensed use limited to: UNIVERSITY NOTRE DAME. Downloaded on February 14,2023 at 18:29:53 UTC from IEEE Xplore. Restrictions apply.

This article has been accepted for publication in IEEE Transactions on Antennas and Propagation. This is the author's version which has not been fully edited and content may change prior to final publication. Citation information: DOI 10.1109/TAP.2023.3240085

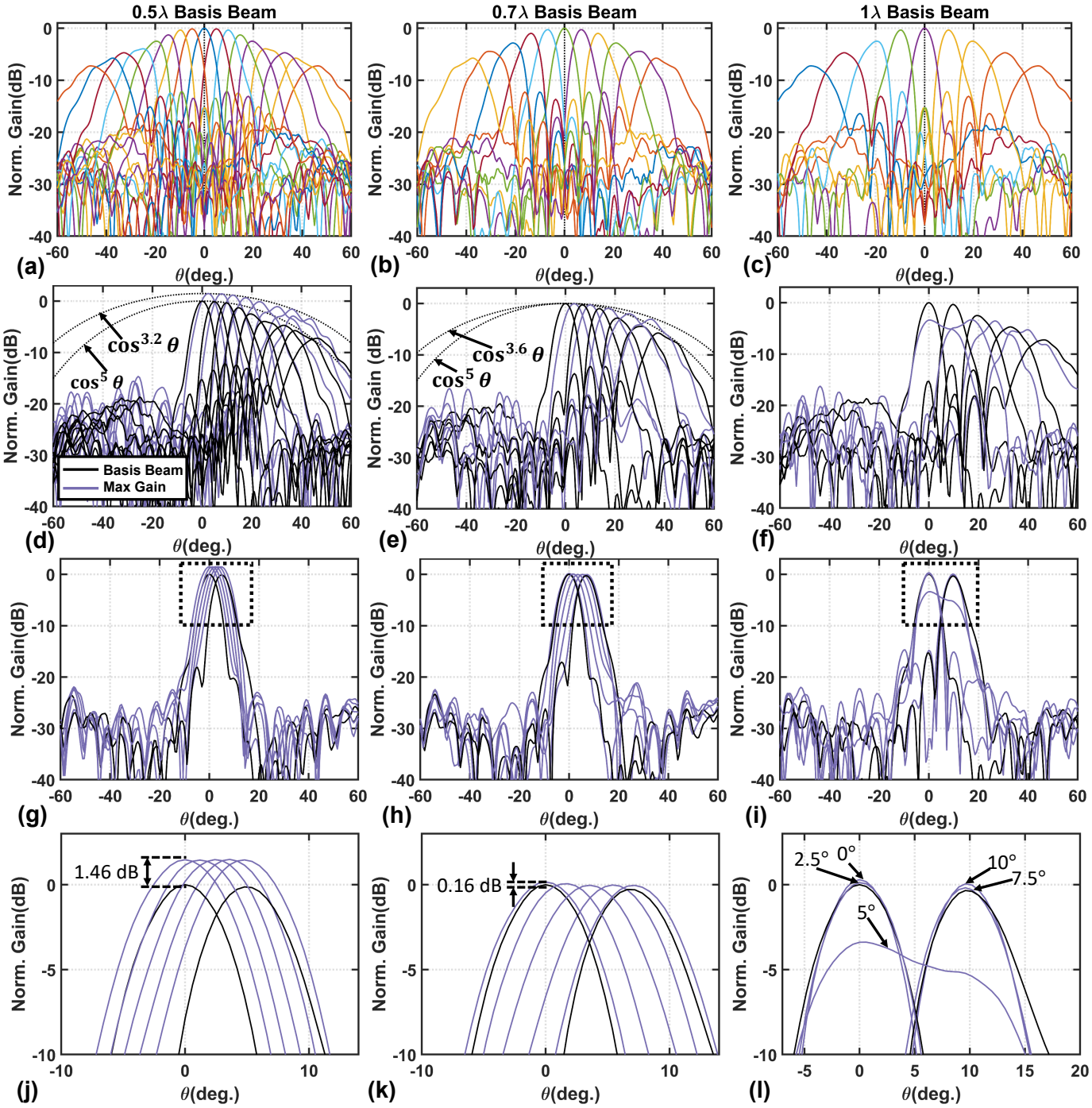

Fig. 4. Beamforming results for uniform linear arrays with three inter-element spacings: 0.5λ in first column, 0.7λ the second column, and 1λ in the third column. The basis beams are shown in (a-c). Perfect symmetry in the bases is observed because beams steered to negative θ were obtained by reflecting beams across $\theta = 0$. Closer array spacing corresponds to greater overlap between beams. Figures (d-f) demonstrate null filling performance using the maximum gain solution out to a $\theta_0 = 40°$. For the 0.5λ and 0.7λ arrays, 'null-steered' beams exhibit equal or greater gain than the original bases, and the beam scan exponent is reduced significantly. Figures (g-i) show beam-scanning near broadside, and figures (j-l) zoom in on the peaks of (g-i). Note that the 1λ–spaced beams show significant gain reduction within the null. Moreover, due to poor beam shape, the gain solver is unable to satisfy the beam-steering requirement, with the maximum gain of synthesized beams observed at $\theta_{max} \neq \theta_0$ (see the 5° beam).

© 2023 IEEE. Personal use is permitted, but republication/redistribution requires IEEE permission. See https://www.ieee.org/publications/rights/index.html for more information.
Authorized licensed use limited to: UNIVERSITY NOTRE DAME. Downloaded on February 14,2023 at 18:29:53 UTC from IEEE Xplore. Restrictions apply.

This article has been accepted for publication in IEEE Transactions on Antennas and Propagation. This is the author's version which has not been fully edited and content may change prior to final publication. Citation information: DOI 10.1109/TAP.2023.3240085

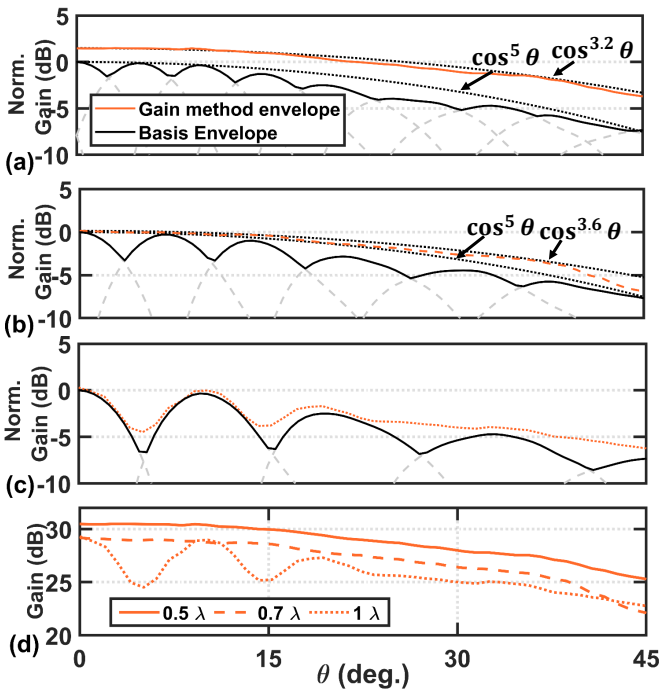

Fig. 5. (a)-(c) Basis beams (dashed gray traces), basis beam envelope (solid black), and synthesized beams using (3) for 0.5λ– , 0.7λ– , and 1λ–spaced feed arrays. The basis envelope exhibits gain ripple due to nulls between fixed basis beams. For 0.5λ spacing, a > 1.5 dB gain and scan loss improvement are achieved over For 0.7λ, both benefits are less dramatic. 1λ spaced feeds exhibit gain ripple due to deep nulls between basis beams.

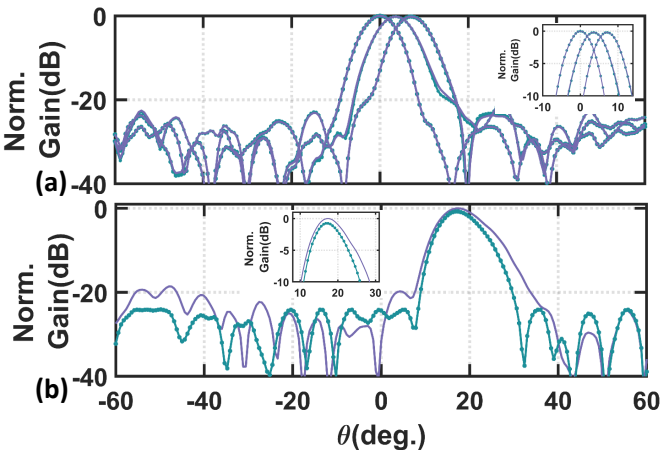

Fig. 6. Comparison of synthesized beams at 0.7λ spacing using PSO and the maximum gain solution. (a) When the PSO method is used with a gain-dominated FoM the PSO beam shape and peak gain values agree well with the max gain solution for all angles. (b) A multi-objective PSO beam synthesis which heavily weights sidelobe level and beamwidth results in a lower gain but a narrower beam with lower sidelobes.

Fig. 7(d)(e)(f) show the patch element model in HFSS in different views. The patch comprises two layers of Rogers RO4350 ($\epsilon_r = 3.66$), separated by a common ground. The upper dielectric layer is 10 mil thick and the lower is 20 mil. Shown on Fig. 7(d), the patch elements are 2.4 mm $\times$ 3.51 mm and pin-fed at an inset location which optimizes input match, which is 1.755 mm and 0.75 mm away from the lower right patch corner in $x-$ and $y-$axis, respectively. Fig. 7(e) shows the bottom feed line connecting the feed pin and SMPM connector. The feed pin transitions to a back-side microstrip line and finally to an SMPM connector footprint. The realized 8-element feed array is a 0.725λ–spaced linear patch array operating at 29 GHz with 3 dBi directivity per feed as shown in Fig. 7(g)(h). The time-gated S11 measurement for all patches is shown in Fig. 7(i) (time gating was used to remove free-space coupling), indicating resonance at 29 GHz. We note that in a practical system larger feed arrays would be necessary in order to address the entire FoV of the lens. To this end any method of phased array design is acceptable including RF, LO, and IF beamformers, full-digital beamformers, and even hybrid arrays.

As stated earlier, one of the benefits of a widely-spaced feed array is the reduction of mutual coupling. In order to confirm the that the mutual coupling is low we have measured the port-to-port coupling $|S_{ij}|$ of the eight-element patch array as shown in Fig. 8(a). Note that an eight-element array has 64 mutual coupling terms but, due to symmetry, only 28 S_{ij} terms and eight S_{ii} terms are plotted. For this 0.725λ–spaced feed array all mutual coupling terms are below -18 dB while simulation of an identically array scaled to 0.5λ–spacing exhibits a worst-case mutual coupling of -12 dB (6 dB higher coupling). Another possible form of mutual coupling in a PAFL system is through reflected power from the ith port, off the bottom of the lens and into the jth port. Figure 8(b) shows the mutual coupling from port one to all other ports $|S_{1j}|\forall j \in [1, 8]$. Solid traces show the S_{1j} without the GRIN lens present and dashed traces are with the GRIN lens present. There is almost no deviation between the two confirming that the mutual coupling via lens reflections is insignificant.

The 4" GRIN lens [see Fig. 9(a)], previously described in [30] has 27.3 dBi broadside gain at 29 GHz when fed with a 10 dBi horn feed from the previous section and a radiation efficiency of 74%. However, in the PAFL configuration it is fed with the 8-element patch array at its approximate focal plane ($F/D = 0.5$). Since the lens is $\sim 10\lambda$ in diameter and the patch array is only 5.075λ wide, two array locations are used in order to record basis beams across the entire field-of-view of the lens, as shown in Fig. 9(b). The complex beam weights of the patch array were produced by an 8-channel Ka-band Satcom transmit beamforming IC evaluation board (IDT F6502) with 8 bits of gain control and 6 bits of phase control. It was confirmed that quantization errors (due to limited number of bits) had a minimal effect on the resulting beams.

All basis beams and synthesized beams were measured using a standard planar near-field scanning system manufactured by NSI-MI (https://www.nsi-mi.com). The system employs standard near-field probing techniques and near-field-to-far-field calculation software to determine the far-field radiation pattern of the test antenna [55]. Figure 7(b) and (c) show the WR28 OEWG near-field (NF) probe in the scan plane, offset 3λ from the front of the GRIN lens.

A. Measurement Setup and Calibration

The theoretical results presented in Section II assume that all feed elements are identical. For any practical (non-ideal)

© 2023 IEEE. Personal use is permitted, but republication/redistribution requires IEEE permission. See https://www.ieee.org/publications/rights/index.html for more information.
Authorized licensed use limited to: UNIVERSITY NOTRE DAME. Downloaded on February 14,2023 at 18:29:53 UTC from IEEE Xplore. Restrictions apply.

This article has been accepted for publication in IEEE Transactions on Antennas and Propagation. This is the author's version which has not been fully edited and content may change prior to final publication. Citation information: DOI 10.1109/TAP.2023.3240085

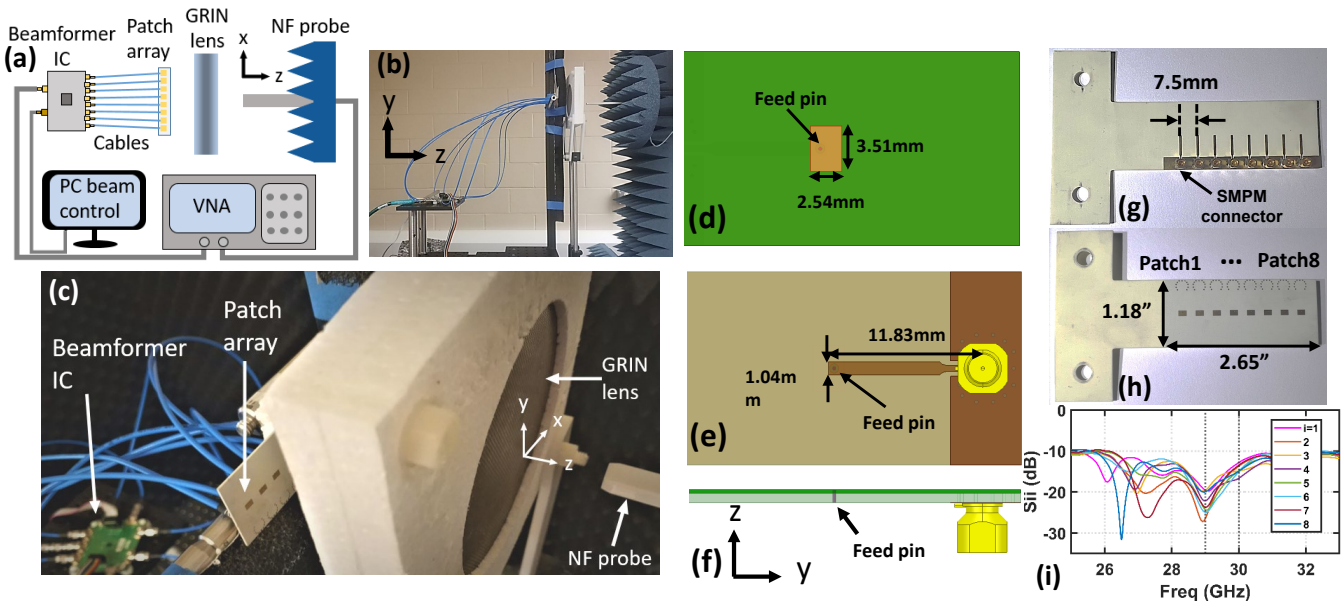

Fig. 7. (a) Measurement setup schematic for the array-fed lens antenna. The pattern is measured by an NSI-MI planar near field scanner. (b) Side view of the measurement setup. (c) A zoom figure of the measurement setup. A single feed array patch element model is shown in (d) top-view (e) bottom-view, and (f) side-view. (g) Bottom-view of the fabricated patch array. (h) Top-view of the fabricated patch array.(i) Measured $|Sii|$ for 8 patches.

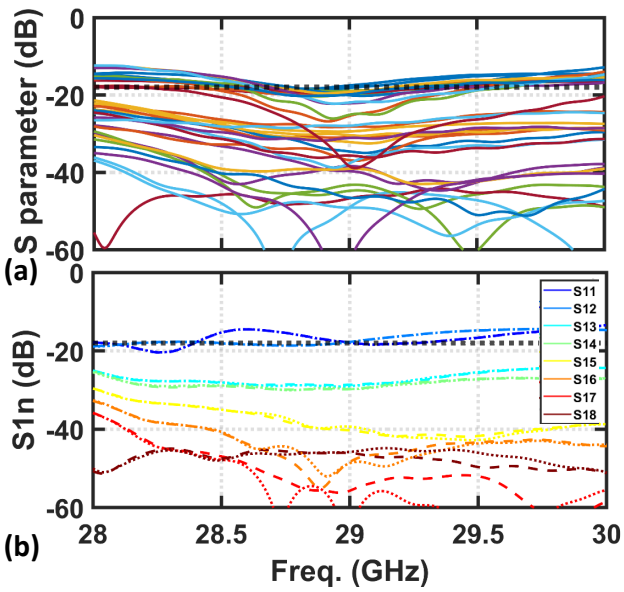

Fig. 8. (a) Mutual coupling $|S_{ij}|$ of the entire eight-element 0.725λ–spaced feed array, omitting redundant measurements. The vertical dashed trace indicates the operating frequency and the horizontal dashed trace is at -18 dB and indicates the worst-case mutual coupling. (b) Passive feed array mutual coupling $|S_{1n}|$ relative to port one, with (dashed) and without (solid) the GRIN lens present.

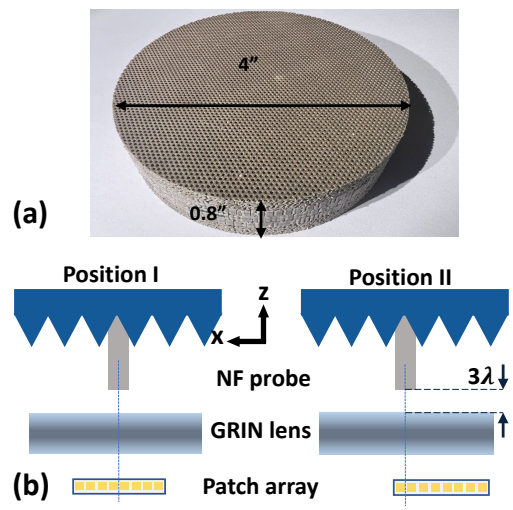

Fig. 9. (a) A photo of the 4" GRIN lens [30]. (b) Basis beam measurement positioning.

system a calibration is necessary to account for antenna loss and imbalances between transmit channels. Equation (1) can be rewritten as,

$$\boldsymbol{e} = \boldsymbol{H}(\boldsymbol{\varepsilon} \circ \boldsymbol{s}), \tag{6}$$

where $\boldsymbol{\varepsilon}$ is a column vector representing per-channel voltage loss and $\circ$ represents the Hadamard product. Due to the imbalance in channels, using (3) directly could result in undesirable beam patterns. Since we are ultimately interested in beam patterns, we use directivity instead of gain as the metric of choice. It can be shown (Appendix B) that maximizing the metric

$$\frac{|\boldsymbol{h}_0 \boldsymbol{s}|^2}{\|\boldsymbol{H}\boldsymbol{s}\|^2} \tag{7}$$

is equivalent to maximizing directivity (for uniform sampling of the radiating sphere in *solid angle*), and furthermore, that the solution to the above using the method of Lagrange multipliers is given by ((33) in Appendix B) and repeated here for convenience:

$$\boldsymbol{s}_{opt,d} = (\boldsymbol{H}^* \boldsymbol{H})^{-1} \boldsymbol{h}_0. \tag{8}$$

© 2023 IEEE. Personal use is permitted, but republication/redistribution requires IEEE permission. See https://www.ieee.org/publications/rights/index.html for more information.
Authorized licensed use limited to: UNIVERSITY NOTRE DAME. Downloaded on February 14,2023 at 18:29:53 UTC from IEEE Xplore. Restrictions apply.

This article has been accepted for publication in IEEE Transactions on Antennas and Propagation. This is the author's version which has not been fully edited and content may change prior to final publication. Citation information: DOI 10.1109/TAP.2023.3240085

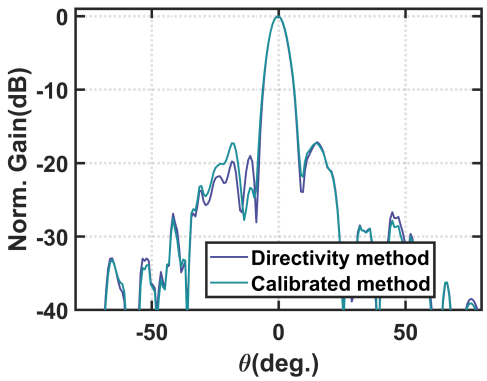

Fig. 10. Theoretical synthesized beams using the calibrated gain solver and the directivity solver show substantial agreement, confirming the suitability of the proposed directivity solver. Five beams are used to synthesize the target beam at $\theta = 0°$.

Although one could directly use (8) for the calculation, (3) is substantially faster than the maximum directivity solution ($\mathcal{O}(N)$ vs. $\sim \mathcal{O}(NM^2)$, where N is the number of antennas and M the number of rows corresponding to sample points on the radiating sphere). This would be particularly important for lens/array co-optimization approaches in which the optimal weights must be computed for any candidate lens design. In order to make (3) for solving for directivity, the *gain metric* should be a maximum at $\boldsymbol{s}_{opt,d}$. If this is true, both algorithms will return the *same weights* and thus the resulting beams will be identical. This can be satisfied by assuming there exists an $\boldsymbol{H}'$ that, when inserted into (3) will return $\boldsymbol{s}_{opt,d}$:

$$\boldsymbol{s}'_{opt,g} = \boldsymbol{h}'^*_0 = (\boldsymbol{H}^*\boldsymbol{H})^{-1}\boldsymbol{h}^*_0 = \boldsymbol{s}_{opt,d}. \tag{9}$$

Solving for $\boldsymbol{H}'$ and making the substitutions that $\boldsymbol{h}_0 = \boldsymbol{g}^T\boldsymbol{H}$ and $\boldsymbol{h}'_0 = \boldsymbol{g}^T\boldsymbol{H}'$, where $\boldsymbol{g}$ is a column vector that consists of all zeros except for the index corresponding to the row denoting the beam steering angle and $[\cdot]^T$ denotes the matrix transpose:

$$\begin{aligned} \boldsymbol{h}'^*_0 &= (\boldsymbol{H}^*\boldsymbol{H})^{-1}\boldsymbol{h}_0 \\ (\boldsymbol{g}^T\boldsymbol{H}')^* &= (\boldsymbol{H}^*\boldsymbol{H})^{-1}(\boldsymbol{g}^T\boldsymbol{H})^* \\ \boldsymbol{H}'^*\boldsymbol{g} &= (\boldsymbol{H}^*\boldsymbol{H})^{-1}\boldsymbol{H}^*\boldsymbol{g} \\ \boldsymbol{H}'^* &= (\boldsymbol{H}^*\boldsymbol{H})^{-1}\boldsymbol{H}^* \\ \boldsymbol{H}' &= \left[(\boldsymbol{H}^*\boldsymbol{H})^{-1}\boldsymbol{H}^*\right]^*. \end{aligned} \tag{10}$$

By making this substitution, we ensure that, regardless of power imbalance between the channels, we will identify weights that maximize *beam quality*. Moreover, this calibrated gain metric can even be used for PSO. In fact, this substitution is equivalent to a version of the maximum directivity solution using a look-up table to speed up execution (i.e., pre-compute $(\boldsymbol{H}^*\boldsymbol{H})^{-1}$). Fig. 10 shows a comparison of 5-feed-synthesized 0° beams using the calibrated gain and directivity solutions. The calibrated weights are: $0.64e^{j93°}$, $0.79e^{j-117°}$, $1e^{j0°}$, $0.97e^{j30°}$, $0.41e^{j-141°}$. The weights given by the maximum directivity solution are: $0.59e^{j81°}$, $0.86e^{j-128°}$, $1e^{j0°}$, $0.92e^{j27°}$, $0.40e^{j-149°}$. Thus the calibrated gain is effectively equivalent to the maximum directivity solution, with error likely due to numerical error from matrix inversion. All measurements involving the maximum gain solution in the following sections implement this *calibrated* gain solution. One of the benefits of this calibration is that it results in an optimal gain for a given PAFL realization without requiring a detailed investigation into loss mechanisms.

B. Null-filling Measurement

To demonstrate measured null-filling, due to the finite fabricated array length, we are not able to use all possible basis for synthesis and must choose an array position for each measurement as shown in Fig. 7(h). The measured basis beams are shown on Fig. 11(a) with a $\pm 55°$ scan range. The broadside basis beam crossover level is -2.5 dB. Note that although the 4-inch lens was initially designed for a 10 dBi horn antenna as the feeding element, these horns are impractical as array elements due to large aperture size. As a result, the patch-fed basis beams are degraded from the horn simulations, especially at the edge of the lens due to radiation spillover. Using the calibrated maximum gain solution beams were synthesized theoretically in the nulls between the measured basis beams, as in Fig. 4(d-f), and the results are shown in Fig. 11(b). The theoretically derived beams are shown in dashed red, which ideally will be identical to the measured synthesized beams in blue, because the theoretical beams are still derived from measured bases. Differences between the measurement and theoretical beams can result from imperfect calibration or temperature variations between basis measurement and beam-scan measurements.

The synthesized beams at 0°, 7.6°, 14.2° and 21.6° are synthesized with the array in Position I, and the beams at 28.4°, 37.6° and 50° are synthesized with the array in Position II (Fig. 9(b)). Complex weights for each scanning angle are provided in Table I. As expected, measured beams are in excellent agreement with the corresponding theoretical beams. The synthesized beam at 0° achieves directivity of 26.65 dB in theory and 26.5 dB in measurement, nearly as high as the two neighboring basis beams with directivities of 26.67 dB and 26.62 dB. In general, as with Fig.4(e), we are able to synthesize beams with directivity commensurate with the basis beams near broadside. Moreover, synthesized beams exhibit a greatly improved scan loss (from $\cos^5(\theta)$ to $\cos^{3.6}(\theta)$). We note that while the proposed method can *improve* scan loss, it cannot produce high directivity at angles where high-directivity basis beams do not exist—in other words, the method is capable of producing maximum directivity at a given angle but the maximum directivity is limited by how much energy the lens is capable of focusing toward that angle. PAFL can improve scan loss in angular regions where basis beams exist (and hence, reduce the scan loss exponent) but it cannot increase the FoV where no basis beams exist.

V. General Beamforming Functionality

The objective of the PAFL is to provide the majority of the functionality expected of a phased array at reduced cost and a fraction of the power. In this section we demonstrate how the proposed system generalizes to other lens designs in

© 2023 IEEE. Personal use is permitted, but republication/redistribution requires IEEE permission. See https://www.ieee.org/publications/rights/index.html for more information.
Authorized licensed use limited to: UNIVERSITY NOTRE DAME. Downloaded on February 14,2023 at 18:29:53 UTC from IEEE Xplore. Restrictions apply.

This article has been accepted for publication in IEEE Transactions on Antennas and Propagation. This is the author's version which has not been fully edited and content may change prior to final publication. Citation information: DOI 10.1109/TAP.2023.3240085

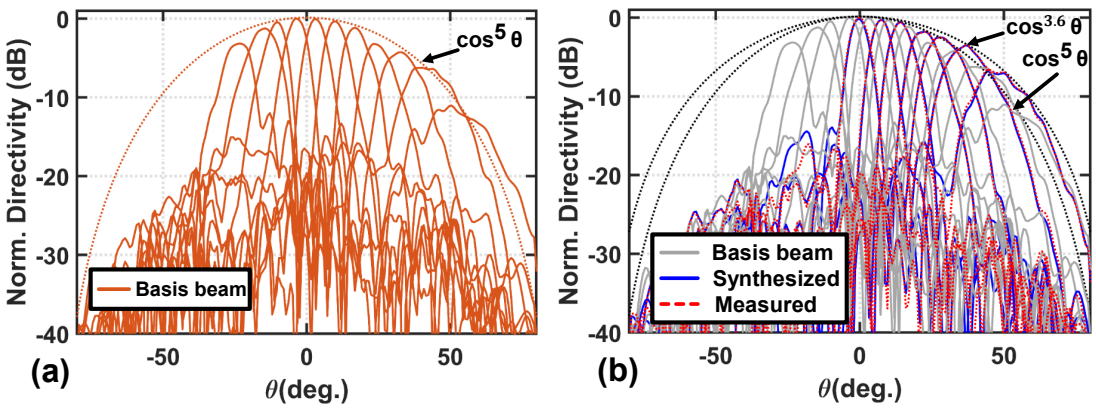

Fig. 11. (a) The measured basis beams at $\phi = 0°$ for the 0.725λ patch array feed follows an approximate $\cos^5(\theta)$ scan loss envelope. (b) Null-filling measurement at angles halfway between adjacent basis beams. The red dashed lines are the theoretical synthesized beams based on measured bases and blue solid lines are measured beams using the prototype system. Each beam is formed using only five basis beams out of eight. Not only can nulls be filled, but directivity increases for beams at large θ, resulting in a lower scan loss exponent (from $n_s = 5$ to $n_s = 3.6$).

TABLE I
COMPLEX FEED WEIGHTS (DB,DEGREES) FOR EACH SCAN ANGLE IN FIG. 11.

Angle (deg)	P1	P2	P3	P4	P5	P6	P7	P8
0	OFF	-3.8 dB$\angle -54.2°$	-2.1$\angle$96.3°	0$\angle$0°	-0.3$\angle -65.7°$	-7.8$\angle -173°$	OFF	OFF
7.6	OFF	OFF	OFF	-12.9$\angle -136.4°$	-2.7$\angle -103.3°$	0$\angle$0°	-5.9$\angle$70.1°	-9.1$\angle$115.7°
14.2	OFF	OFF	OFF	-17.8$\angle -104.9°$	-19.7$\angle$78.3°	-1.1$\angle$17.3°	0$\angle$0°	-6.2$\angle$101.4°
21.6	OFF	OFF	OFF	-19.9$\angle -160°$	-13.2$\angle$125.4°	-17.3$\angle$5.8°	-2.9$\angle$135.5°	0$\angle$0°
28.4	OFF	OFF	-26.7$\angle -117.1°$	OFF	0$\angle$0°	-1.2$\angle -25.4°$	-14.7$\angle -128°$	-14.5$\angle -67°$
37.6	OFF	OFF	OFF	-13.5$\angle -60.3°$	-9$\angle -70°$	0$\angle$0°	-1.3$\angle$109.9°	-12.2$\angle -1.3°$
50	-14.5$\angle -52.7°$	-19.7$\angle -15.2°$	OFF	OFF	OFF	-8$\angle -150.2°$	-0.5$\angle$173.8°	0$\angle$0°

the literature and can realize the following critical functions for current and future wireless millimeter-wave beam-scanning systems:

- formation of beams at arbitrary angles (already shown above),
- control of beam shape, especially sidelobe level and coma-lobe suppression,
- multibeam operation, especially for make-before-break applications,
- broad-beam synthesis for e.g., beam search.

We now show that the PAFL provides the last three capabilities. Beams are synthesized using basis beams in Fig. 11(a).

A. Improved beam shape

Improved beam shape can be achieved by taking advantage of the PSO algorithm's greater degrees of freedom, especially as the target beam angle increases. In Fig. 12, two examples are shown to demonstrate beams optimized specifically for SLL and beamwidth (BW), with active feeds consisting of the optimal six as chosen via a brute force selection method. The brute force method uses the PSO optimization for all possible combinations of six active feeds and selects the feeds for which the resulting synthesized beam has the maximum FoM. Due to the differences in the component FoM functionals $V(\boldsymbol{Hs})$, because each L_i was set to be equal for each f_i, some component FoMs accrue significantly more or less error for the same empirical difference in beam quality, and thus the weights were empirically tuned to accentuate particular beam features. The first example in Fig. 12(a) uses a relatively high w_{SLL}. The beam is targeted at $\theta = 50°$, and the realized PSO beam SLL is at least 10.6dB better than beams synthesized using the maximum gain solution. Fig. 12(b) shows a $\theta = 37°$ beam synthesized with a high w_{BW}. The realized beam is 2.6° narrower at its 6 dB point and 4.2° narrower at its 10 dB point than that synthesized using the calibrated maximum gain solution.

B. Multibeam operation

As neither of our algorithms can directly synthesize multiple beams, we rely here on superposition, reasoning that two narrow beams with a sufficient angular separation should minimally interact. Two beams are initially synthesized separately using 3 feeds at -23° (using patches 1-3) and 23° (using patches 6-8), near the measured basis nulls at -20.3° and 21.6°. Then the two sets of weights are normalized for equal power in each beam and the beams are excited simultaneously. Figure 13 shows the resulting multibeam pattern, and compares this pattern with the original -23° and 23° beams. The result shows good agreement between simulation and measurement, and the main lobes of the originally synthesized beams are not much changed by the simultaneous beam excitation. This is due to the directional element patterns and the correspondingly low number of active feeds necessary for a given beam. It is important to note that while we chose to synthesize beams at

© 2023 IEEE. Personal use is permitted, but republication/redistribution requires IEEE permission. See https://www.ieee.org/publications/rights/index.html for more information.
Authorized licensed use limited to: UNIVERSITY NOTRE DAME. Downloaded on February 14,2023 at 18:29:53 UTC from IEEE Xplore. Restrictions apply.

This article has been accepted for publication in IEEE Transactions on Antennas and Propagation. This is the author's version which has not been fully edited and content may change prior to final publication. Citation information: DOI 10.1109/TAP.2023.3240085

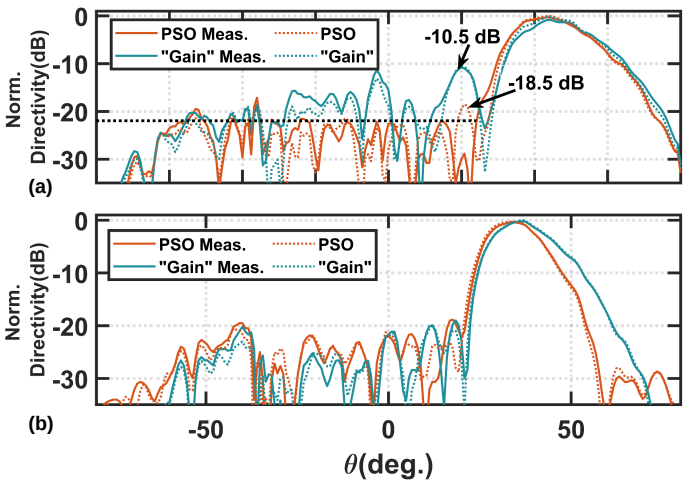

Fig. 12. Beam shaping examples focusing on (a) SLL and (b) beamwidth (BW). Dashed lines denote simulated results and solid lines denote measured results. In (a), the target angle is 50° and the PSO beam exhibits -7.6 dB better SLL than the maximum gain solution. In (b), the target angle is at 37° and the PSO beam has a 2.6° narrower 6-dB BW and a 4.2° narrower 10-dB BW than the maximum gain solution, while only losing 0.2 dB in directivity.

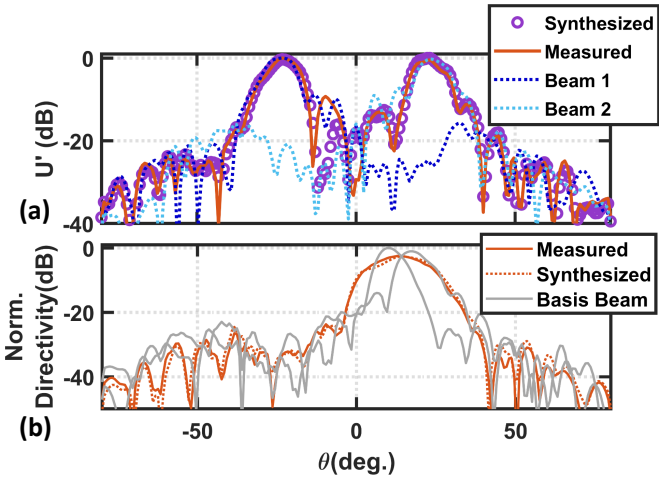

Fig. 13. (a) Synthesized pattern has beams at both -23° and 23°. The relatively large angular separation for this multibeam pattern minimally affects the beam shape. (b) A synthesized beam with a wide 3dB beam width of 17.6° where the closest two basis beams have 7.7° and 8.7° 3dB beam widths.

$\pm 23°$, the beams angles can be completely arbitrary at (θ_i, ϕ_i) and (θ_j, ϕ_j) where $\theta_i \neq \theta_j$ and $\phi_i \neq \phi_j$.

C. Broad Beam Synthesis

One strategy to reduce network latency in multi-antenna systems is to employ an iterative search using progressively narrower beams during channel characterization [56]. Again, since our algorithms are designed for high-gain pencil beams, we resort to a heuristic approach to beamforming. Fig. 13(b) shows a synthesized 17.6° 3dB-beamwidth beam at 13.6°, using in-phase excitation of patches 5-8 in array Position I. Two basis beams are plotted for comparison, with 3dB-beamwidths of 7.7° and 8.7°.

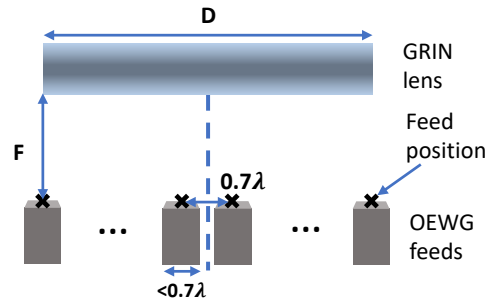

Fig. 14. Schematic of full-wave simulation showing an OEWG array feeding three lenses from the literature ([30], [28], [20]). The OEWG feed width is $< 0.7\lambda$ so it can fit on a 0.7 or 0.8λ–spaced grid. Corresponding normalized gain is shown in Fig. 15(a)–(d). Only two edge feeds are shown for clarity. Simulation details are listed in Tab. II.

D. Beamforming with Various State-of-the-art Lenses

To demonstrate the general applicability of beamforming techniques to PAFL systems, we investigated two additional GRIN designs from the literature: [20] and a $F/D = 0.5$ version of [28]. A 3D FDTD full-wave simulator (Empire XPU) was used to simulate the basis beams using a practically realizable open-ended waveguide (OEWG) feed array as shown in Fig. 14. The F/D reduction was necessary for the latter design because the original (large) F/D exhibited a severely reduced FoV. The $F/D = 0.5$ version was generated with the design equations [28], and broadside gain was confirmed to be in agreement with the reported value.

It is worth noting that neither [20] nor [28] were explicitly designed for beam-scanning performance, and therefore have significant scan loss. Our in-house lens [30] was also simulated using an OEWG array for easier comparison in performance improvement with gain solvers. Table II describes the details for these lens simulations. Due to F/D and feeding differences between the simulated and published lenses, the results shown here are purely for illustrating the potential improvement from using the beamforming methods proposed in this work and are not necessarily indicative of the full performance capabilities of these lenses as originally designed.

Figure 15(a), (c), and (d) show substantial improvement in scan loss is possible for all lenses using a 0.7λ–spaced feed array, with up to 1.8 dB increase in broadside gain (corresponding to a scan-loss exponent improvement from $n_s \rightarrow n_s - 2$). This represents a gain improvement of up to 4 dB in the case of [20] at 40°. Fig. 15(a) and (b) provide a comparison of gain improvement using 0.7λ and 0.8λ feed spacing for the lens reported in [30]. For 0.8λ–spaced feeds [Fig. 15(b)] the PAFL scan-loss exponent $n_s = 5$ is worse than the 0.7λ–spaced feed scan-loss exponent, $n_s = 4$ (consistent with results from Section III).

As mentioned earlier, while the PAFL method is able to improve the scan loss of arbitrary lenses, it is only capable of improving upon the basis beams that are actually inherent to the lens itself. If a given lens does not produce a high-directivity beam at a given angle PAFL cannot produce significant radiation at that angle. The lens should first be designed to have low scan loss over the FoV and then PAFL can further improve performance.

© 2023 IEEE. Personal use is permitted, but republication/redistribution requires IEEE permission. See https://www.ieee.org/publications/rights/index.html for more information.
Authorized licensed use limited to: UNIVERSITY NOTRE DAME. Downloaded on February 14,2023 at 18:29:53 UTC from IEEE Xplore. Restrictions apply.

This article has been accepted for publication in IEEE Transactions on Antennas and Propagation. This is the author's version which has not been fully edited and content may change prior to final publication. Citation information: DOI 10.1109/TAP.2023.3240085

TABLE II
DETAILS FOR THE LENS SIMULATIONS FROM LITERATURE, AS SHOWN IN FIG. 15

	As simulated in this work									As originally published				
Lens	F	D (λ)	F/D (λ)	spacing	Freq. (λ)	# of feeds (GHz)	OEWG	scan loss	scan loss (w/ PAFL)	Freq. (GHz)	F (λ)	D (λ)	F/D	Feed
[30]	4.3	9.0	0.5	0.7	26.5	14	WR-28	$\cos^6(\theta)$	$\cos^4(\theta)$	26.5	4.3	9	0.5	Horn
[30]	4.3	9.0	0.5	0.8	26.5	12	WR-28	$\cos^6(\theta)$	$\cos^5(\theta)$	26.5	4.3	9	0.5	Horn
[28]	2.5	5.0	0.5	0.7	12.4	8	WR-62	$\cos^5(\theta)$	$\cos^4(\theta)$	40	20	16	1.25	OEWG
[20]	2.4	4.1	0.6	0.7	12.4	8	WR-62	$\cos^{4.5}(\theta)$	$\cos^3(\theta)$	13.4	3	5	0.6	Patch

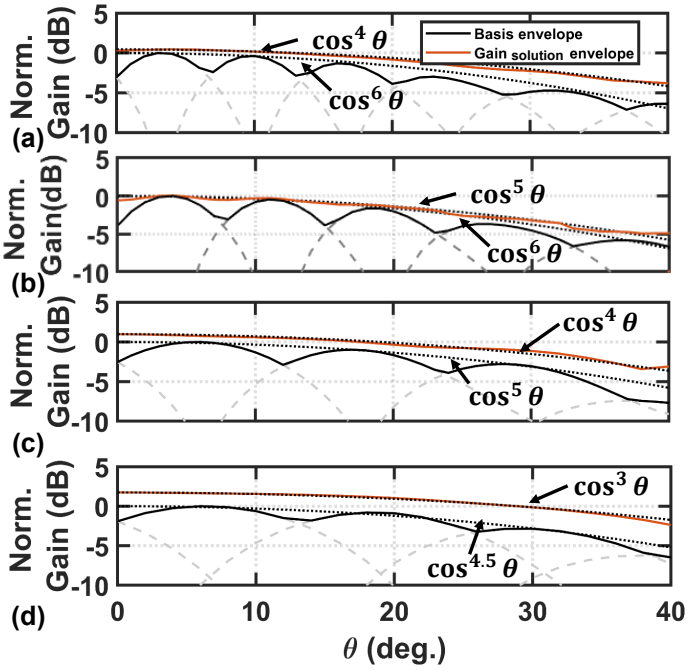

Fig. 15. Improvement in beamscan performance and scan loss exponent using (3) for various lenses reported in the literature. (a) [30] at 0.7λ spacing, (b) [30] at 0.8λ spacing, (c) [28] at 0.7λ spacing, and (d) [20] at 0.7λ spacing. Lenses are excited by OEWGs as shown in Fig. 14.

To achieve even better scan loss the lens could be jointly optimized with the PAFL method in the loop. That is, the GRIN profile of the lens as well as feed array element pattern and spacing could be optimized subject to the condition that the lens is fed with optimal weights from (3) and using the "loudest neighbor" heuristic (from Appendix A). These closed form expressions are amenable to rapid optimization loops but should be combined with a correspondingly rapid EM solver such as those based on curved-ray geometrical optics [57] with diffraction [58]. Joint design of the entire PAFL system is the subject of future investigation.

VI. CONCLUSIONS AND FUTURE WORK

This work has shown that a widely-spaced (>0.5λ) phased array behind a practical lens antenna can eliminate many of the problems exhibited by switch-beam systems. For the prototype used herein, gain-droop between bases is removed and scan loss is substantially reduced (up to 4 dB), with only a very small number (e.g., 5) of active feeds. PAFL concept generality is demonstrated by simulating several systems employing state-of-the-art lenses in the literature, with similar improvement in null-filling and beam-scan. A multi-objective optimizer based upon PSO was presented to control beam-shape, which uses the optimal gain solution for calibration, benchmarking, and particle seeding. An PAFL system is thus shown to use significantly fewer elements than an equivalent phased-array ($n << P$) and consuming a small fraction of the power. However, it should be noted this also reduces EIRP relative to an equivalently sized PAA. For example, if the beamformer IC used in this work were driven at 1 dB compression (OP1dB=11 dBm/channel), the complex weights used for a broadside beam would produce an EIRP of 42.6 dBm. At around 30 degrees the EIRP would drop to 37.7 dBm and at 50 degrees it would be 34 dBm. This low EIRP is due to the low output power of silicon and the small number of active feeds used in the PAFL method. Higher EIPR could be achieved by using a high-power beamformer ICs (using e.g., GaN) and by defocusing the feed array (a lower F/D) to increase n, the number of active elements used to form a beam.

Lens design for explicit use in a PAFL system are beyond the scope of this work. However, we observe that PAFL beam-scan performance is improved if the lens itself exhibits low scan loss. Thus, PAFL systems will benefit from research into improved beam-scanning lens designs, especially for lenses with a flat form factor. Moreover, explicitly low-complexity, low-cost lens designs may be considered. As has been shown, PSO beamforming can greatly improve the performance of lenses with relatively poor beamscan performance, and if PAFL algorithms were used with an explicitly simplified lens geometry (e.g., a very coarsely-discretized version of [28]), the result could a be a very low-cost, low scan-loss PAFL system.

Although this work only considered a uniform array parameterized on inter-element spacing, many more factors may be considered in future feed-array design. For example, with more space for each feed element, alternative (e.g., wideband) antennas can be considered which may not fit in a 0.5λ grid. Element-to-element coupling is also reduced, which could solve issues related to scan blindness. Or, given the fewer number of feed elements and the significant reduction in active feed elements, full digital beamforming architectures may become more compelling due to a reduced number of ADCs and lower-complexity baseband processing. Another possibility is to grade the feed spacing to reduce cost/complexity. As was shown, null-filling is ultimately governed by gain crossover of the basis beams and therefore wider basis beams allow for

© 2023 IEEE. Personal use is permitted, but republication/redistribution requires IEEE permission. See https://www.ieee.org/publications/rights/index.html for more information.
Authorized licensed use limited to: UNIVERSITY NOTRE DAME. Downloaded on February 14,2023 at 18:29:53 UTC from IEEE Xplore. Restrictions apply.

This article has been accepted for publication in IEEE Transactions on Antennas and Propagation. This is the author's version which has not been fully edited and content may change prior to final publication. Citation information: DOI 10.1109/TAP.2023.3240085

wider spacing of feed elements. Since, for planar aperture antennas, beams broaden as scan angle increases it may be possible to use wider-spaced feeds at the edge of the feed array to further reduce the number of elements.

For each of the above tradeoffs, a joint optimization is needed in which a lens is designed and evaluated for the maximum possible gain over scan for that given lens realization. The proposed numerically efficient methods for computing maximum gain as well as the "loudest neighbor" (see Appendix A) heuristic are critical to lens/feed-array joint optimization. Taken together the methods in this work allow for the rapid calculation of maximum gain versus scan angle for a candidate PAFL system.

Appendix A
Proof of Maximum Gain Beamforming

This algorithm provides a feed weight vector $\boldsymbol{s}$ such that the maximum possible gain is achieved at a particular target angle (θ_0, ϕ_0). While it is especially important to achieve maximum gain between basis beams (in the nulls) the result is valid at all angles including at basis beams. Gain, in terms of the far-field electric field and the feed weights is,

$$G(\theta,\phi) = \frac{4\pi U(\theta,\phi)}{P_{\text{in}}} = \frac{4\pi U(\theta,\phi)}{\|\boldsymbol{s}\|^2} = \frac{4\pi R^2 |\boldsymbol{E}(\theta,\phi)|^2}{2\eta\|\boldsymbol{s}\|^2}, \tag{11}$$

where $\|\cdot\|$ denotes the L_2 norm.

In (2) there are two rows for a given angle, one for each orthogonal polarization, throughout the remainder of this work we consider only the E_ϕ component and thus can operate upon a single row. In order to solve for an arbitrary polarization an appropriate change of coordinates can be made to collapse (2) to a single row for each polarization. The row corresponding to the desired angle and polarization is $\boldsymbol{h}_0$:

$$\boldsymbol{h}_0 = \begin{bmatrix} E_{\phi,1}(\theta_0,\phi_0) & \dots & E_{\phi,N}(\theta_0,\phi_0) \end{bmatrix}, \tag{12}$$

and

$$G(\theta_0,\phi_0) = \frac{4\pi R^2 |\boldsymbol{h}_0\boldsymbol{s}|^2}{2\eta\|\boldsymbol{s}\|^2}. \tag{13}$$

Since $4\pi R^2/2\eta$ is a constant, there exist two strategies for maximizing $G(\theta_0,\phi_0)$:

1) maximizing $|\boldsymbol{h}_0\boldsymbol{s}|^2$ while keeping $\|\boldsymbol{s}\|^2$ constant, or
2) minimizing $\|\boldsymbol{s}\|^2$ while keeping $|\boldsymbol{h}_0\boldsymbol{s}|^2$ constant,

and finding the feed weights for maximum gain at the target angle is a constrained optimization problem. In the following the second strategy is pursued. Using the Lagrange multiplier method the field value at the steering angle is constrained to an as-yet-undetermined constant ($k = \boldsymbol{h}_0\boldsymbol{s} = E(\theta_0,\phi_0)$) and $\|\boldsymbol{s}\|^2$ is minimized. The Lagrangian of the system is

$$\begin{aligned} \mathcal{L} &= \|\boldsymbol{s}\|^2 + \lambda(\boldsymbol{h}_0\boldsymbol{s} - k) \\ &= \boldsymbol{s}^*\boldsymbol{s} + \lambda(\boldsymbol{h}_0\boldsymbol{s} - k), \end{aligned} \tag{14}$$

which, when minimized yields,

$$\begin{aligned} \nabla\mathcal{L} &= \boldsymbol{s}^* + \lambda\boldsymbol{h}_0 \\ 0 &= \boldsymbol{s} + \lambda\boldsymbol{h}_0^* \\ \boldsymbol{s} &= -\lambda\boldsymbol{h}_0^*, \end{aligned} \tag{15}$$

where λ denotes the Langrange multiplier (a free parameter) and $(\cdot)^*$ denotes the Hermitian transpose operator. From the equality constraint:

$$\begin{aligned} k &= -\lambda\boldsymbol{h}_0\boldsymbol{h}_0^*, \text{ and} \\ \lambda &= \frac{-k}{\boldsymbol{h}_0\boldsymbol{h}_0^*}. \end{aligned} \tag{16}$$

Substituting (16) into (15) yields:

$$\boldsymbol{s} = \frac{k\boldsymbol{h}_0^*}{\boldsymbol{h}_0\boldsymbol{h}_0^*}. \tag{17}$$

Since k has not yet been chosen, it can be used to cancel the scalar factor of $\boldsymbol{h}_0\boldsymbol{h}_0^*$ in the denominator, yielding the straightforward result:

$$\boldsymbol{s} = \boldsymbol{h}_0^*, \tag{18}$$

which is similar to the conjugate field matching approach used in [37]–[40] except that instead of requiring the fields in the focal plane (often a difficult quantity to measure), this result only requires the complex far-fields at the desired angle (a much more straightforward quantity to acquire). In words, in order to form a beam with the highest gain at a particular angle, not only should the antenna phases be set such that all radiation adds coherently at the angle of interest, but each feed should be excited *in proportion to the magnitude of their respective electric field at the steering angle*.

The above result uses all available feed elements represented in $\boldsymbol{s}$ but it is often sufficient (and preferred) to use a small subset of feeds in order that the beamformer ICs for inactive feeds can be disabled to reduce static power consumption (see crossed-out beamformer ICs in Fig. 1(c)). It is now shown that when synthesizing a beam with maximum gain using a *subset* $\boldsymbol{\sigma}$ of feeds, with cardinality $|\boldsymbol{\sigma}| < N$ (corresponding to sub-selected columns of $\boldsymbol{H}$), the feeds which produce the highest amplitude fields at the desired angle (referred to as the "loudest neighbors") should be used. Inserting (18) into (13) yields the optimal gain in the target direction:

$$\begin{aligned} G_0 &= \frac{4\pi R^2 |\boldsymbol{h}_0\boldsymbol{h}_0^*|^2}{2\eta\|\boldsymbol{h}_0\|^2} \\ &= \frac{4\pi R^2 \|\boldsymbol{h}_0\|^4}{2\eta\|\boldsymbol{h}_0\|^2} \\ &= \frac{4\pi R^2 \|\boldsymbol{h}_0\|^2}{2\eta} = \alpha\|\boldsymbol{h}_0\|^2. \end{aligned} \tag{19}$$

Using (19) and the subset $\boldsymbol{\sigma}$:

$$G_{0,\boldsymbol{\sigma}} = \alpha\|\boldsymbol{h}_{0,\boldsymbol{\sigma}}\|^2 = \alpha\sum_{m=1}^{|\boldsymbol{\sigma}|} |h_{0,m}|^2, \tag{20}$$

© 2023 IEEE. Personal use is permitted, but republication/redistribution requires IEEE permission. See https://www.ieee.org/publications/rights/index.html for more information.
Authorized licensed use limited to: UNIVERSITY NOTRE DAME. Downloaded on February 14,2023 at 18:29:53 UTC from IEEE Xplore. Restrictions apply.

This article has been accepted for publication in IEEE Transactions on Antennas and Propagation. This is the author's version which has not been fully edited and content may change prior to final publication. Citation information: DOI 10.1109/TAP.2023.3240085

where $\boldsymbol{h}_{0,\boldsymbol{\sigma}}$ denotes $\boldsymbol{h}_0$ truncated to only include the columns corresponding to $\boldsymbol{\sigma}$ (1-by-$|\boldsymbol{\sigma}|$ vector). Since (20) is a sum of positive numbers:

1) Removing any feed with $|h_{0,n}| \neq 0$ from $\boldsymbol{\sigma}$ reduces $G_{0,\boldsymbol{\sigma}}$
2) Keeping the feeds with highest $|h_{0,n}|$ maximizes the partial sum of (20) and minimizes the reduction of $G_{0,\boldsymbol{\sigma}}$ as feeds are removed.

The second observation is referred to as "loudest neighbor" selection. It is optimal for the maximum gain solution and a useful heuristic when another synthesis algorithm is employed such as Particle Swarm Optimization (PSO) with FoMs other than maximum gain. Though the max gain algorithm cannot itself provide satisfactory beams at large scan angles, it is invaluable for benchmarking and is used to improve the runtime of the implemented PSO discussed below.

Appendix B
Directivity Calibration

Here we cast the directivity maximization into a constrained optimization problem as with the gain maximization (Section A). Let us start with the definition of directivity:

$$D = \frac{U(\theta,\phi)}{\tilde{U}} = \frac{4\pi U(\theta,\phi)}{P_{rad}}. \tag{21}$$

P_{rad} is calculated by integrating the radiant intensity over the far-field sphere:

$$P_{rad} = \oiint_{\Omega} U d\Omega. \tag{22}$$

Representing U in terms of the electric fields measured at a spherical surface at some distance R,

$$U(\theta,\phi) \approx \frac{R^2}{2\eta}(|E_\theta(\theta,\phi)|^2 + |E_\phi(\theta,\phi)|^2), \tag{23}$$

and substituting back into the integral:

$$P_{rad} = \frac{R^2}{2\eta}\left[\oiint_{\Omega} |E_\theta(\theta,\phi)|^2 d\Omega + \oiint_{\Omega} |E_\phi(\theta,\phi)|^2 d\Omega\right]. \tag{24}$$

The above integral can be approximated by a Riemann sum. Assuming $E(\theta,\phi)$ is represented as a vector $\boldsymbol{e}$ uniformly sampled in solid angle yields:

$$P_{rad} \approx \frac{4\pi}{M}\sum_{m=1}^{M} U_m = \frac{2\pi R^2}{M\eta}\sum_{m=1}^{M}|e_m|^2, \tag{25}$$

where M is the total number of elements of $\boldsymbol{e}$. Uniform sampling in (θ,ϕ) (as opposed to solid angle) can be accommodated by explicitly including the spherical differential surface area element in the integral over power density, but we make the above assumption for notational simplicity. By employing (1), we get the following:

$$P_{rad} \approx \frac{2\pi R^2}{M\eta}\|\boldsymbol{e}\|^2 = \frac{2\pi R^2}{M\eta}\|\boldsymbol{H}\boldsymbol{s}\|^2. \tag{26}$$

We now simplify D at a target angle (θ_0,ϕ_0), making the same polarization assumption as Section A and using (12):

$$D = \frac{MU_{\theta_0,\phi_0}}{\|\boldsymbol{H}\boldsymbol{s}\|^2} = \frac{M|e_{\theta_0,\phi_0}|^2}{\|\boldsymbol{H}\boldsymbol{s}\|^2} = \frac{M|\boldsymbol{h}_0\boldsymbol{s}|^2}{\|\boldsymbol{H}\boldsymbol{s}\|^2}. \tag{27}$$

Since $4M$ is a constant, maximizing D consists of keeping constant $|\boldsymbol{h}_0\boldsymbol{s}|^2$ and minimizing $\|\boldsymbol{H}\boldsymbol{s}\|^2$. Specifically:

$$\boldsymbol{h}_0\boldsymbol{s} = k. \tag{28}$$

Using Lagrange multipliers, as in the gain solution, to solve for the beam weights gives the highest possible directivity.

$$\begin{aligned} \mathcal{L} &= \|\boldsymbol{H}\boldsymbol{s}\|^2 + \lambda(\boldsymbol{h}_0\boldsymbol{s} - k) \\ \nabla\mathcal{L} &= \nabla(\boldsymbol{s}^*\boldsymbol{H}^*\boldsymbol{H}\boldsymbol{s}) + \nabla(\lambda\boldsymbol{h}_0\boldsymbol{s} - \lambda k) \\ 0 &= \boldsymbol{H}^*\boldsymbol{H}\boldsymbol{s} + \lambda\boldsymbol{h}_0^*. \end{aligned} \tag{29}$$

Rearranging to solve for $\boldsymbol{s}$:

$$\boldsymbol{s} = -\lambda(\boldsymbol{H}^*\boldsymbol{H})^{-1}\boldsymbol{h}_0^*. \tag{30}$$

Next, k and λ which satisfy the relation are, from (28):

$$\begin{aligned} k &= -\lambda\boldsymbol{h}_0(\boldsymbol{H}^*\boldsymbol{H})^{-1}\boldsymbol{h}_0^* \\ \lambda &= \frac{-k}{\boldsymbol{h}_0(\boldsymbol{H}^*\boldsymbol{H})^{-1}\boldsymbol{h}_0^*}. \end{aligned} \tag{31}$$

Substituting (31) into (30) yields:

$$\boldsymbol{s} = \frac{k(\boldsymbol{H}^*\boldsymbol{H})^{-1}\boldsymbol{h}_0^*}{\boldsymbol{h}_0(\boldsymbol{H}^*\boldsymbol{H})^{-1}\boldsymbol{h}_0^*}. \tag{32}$$

Since the denominator is a scalar, k may be chosen to cancel the denominator, yielding the simpler relation:

$$\boldsymbol{s}_{opt,d} = (\boldsymbol{H}^*\boldsymbol{H})^{-1}\boldsymbol{h}_0^*, \tag{33}$$

which, in the general case in which $\boldsymbol{H}$ is full rank is equivalent to taking a column from the pseudoinverse of $\boldsymbol{H}$. More or less radiated power can be achieved by multiplying $\boldsymbol{s}_{opt,d}$ by a scalar. To see why k is an arbitrary parameter, consider the scaling of k by some parameter α. From (28):

$$\begin{aligned} \alpha\boldsymbol{h}_0\boldsymbol{s}_{opt} &= \alpha k \\ \boldsymbol{h}_0\boldsymbol{s}_{opt,\alpha} &= \alpha k, \text{where} \\ \boldsymbol{s}_{opt,\alpha} &= \alpha\boldsymbol{s}_{opt}. \end{aligned} \tag{34}$$

Substituting into (27):

$$\begin{aligned} D &= \frac{M|\boldsymbol{h}_0\boldsymbol{s}|^2}{\|\boldsymbol{H}\boldsymbol{s}\|^2} = \frac{M|k|^2}{\|\boldsymbol{H}\boldsymbol{s}_{opt}\|^2} \\ D_\alpha &= \frac{M|\boldsymbol{h}_0\boldsymbol{s}|^2}{\|\boldsymbol{H}\boldsymbol{s}_{opt,\alpha}\|^2} = \frac{M|\alpha|^2|k|^2}{|\alpha|^2\|\boldsymbol{H}\boldsymbol{s}_{opt}\|^2} = D. \end{aligned} \tag{35}$$

Thus, optimal directivity is invariant under the choice of k. The same argument is employed for gain in Appendix A.

© 2023 IEEE. Personal use is permitted, but republication/redistribution requires IEEE permission. See https://www.ieee.org/publications/rights/index.html for more information.
Authorized licensed use limited to: UNIVERSITY NOTRE DAME. Downloaded on February 14,2023 at 18:29:53 UTC from IEEE Xplore. Restrictions apply.

This article has been accepted for publication in IEEE Transactions on Antennas and Propagation. This is the author's version which has not been fully edited and content may change prior to final publication. Citation information: DOI 10.1109/TAP.2023.3240085

ACKNOWLEDGEMENT

We gratefully acknowledge support from Renesas Electronics America who supplied the Ka-band SATCOM beamformer IC used in this demonstration. We also thank Mr. Ken Hersey, Dr. Tom Comberiate, and Mr. James McKnight for fruitful discussion regarding phased-array-fed lens antennas.

REFERENCES

[1] P. Hindle, "Comprehensive survey of commercial mmwave phased array companies," *Microwave Journal*, Jan 2020 [Online] www.microwavejournal.com/articles/33357-comprehensive-survey-of-commercial-mmwave-phased-array-companies.

[2] G. Gültepe and G. M. Rebeiz, "A 256-Element Dual-Beam Polarization-Agile SATCOM Ku-Band Phased-Array With 5-dB/K G/T," *IEEE Trans. Microw. Theory Techn.*, pp. 1–1, 2021.

[3] K. Kibaroglu, M. Sayginer, T. Phelps, and G. M. Rebeiz, "A 64-Element 28-GHz Phased-Array Transceiver With 52-dBm EIRP and 8–12-Gb/s 5G Link at 300 Meters Without Any Calibration," *IEEE Trans. Microw. Theory Techn.*, vol. 66, pp. 5796–5811, Dec. 2018.

[4] A. H. Aljuhani, T. Kanar, S. Zihir, and G. M. Rebeiz, "A 256-Element Ku-Band Polarization Agile SATCOM Transmit Phased Array With Wide-Scan Angles, Low Cross Polarization, Deep Nulls, and 36.5-dBW EIRP per Polarization," *IEEE Trans. Microw. Theory Techn.*, vol. 69, pp. 2594–2608, May 2021.

[5] X. Luo, J. Ouyang, Z.-H. Chen, Y. Yan, L. Han, Z. Wu, T. Yu, and K. Zheng, "A Scalable Ka-Band 1024-Element Transmit Dual-Circularly-Polarized Planar Phased Array for SATCOM Application," *IEEE Access*, vol. 8, pp. 156084–156095, 2020.

[6] L. Gao and G. M. Rebeiz, "A 22-44-GHz Phased-Array Receive Beamformer in 45-nm CMOS SOI for 5G Applications With 3-3.6-dB NF," *IEEE Trans. Microw. Theory Techn.*, pp. 1–1, 2020.

[7] Y. Yin, S. Zihir, T. Kanar, Q. Ma, H. Chung, L. Gao, and G. M. Rebeiz, "A 37-42-GHz 8x8 Phased-Array With 48-51-dBm EIRP, 64-QAM 30-Gb/s Data Rates, and EVM Analysis Versus Channel RMS Errors," *IEEE Trans. Microw. Theory Techn.*, pp. 1–1, 2020.

[8] A. H. Aljuhani, T. Kanar, S. Zihir, and G. M. Rebeiz, "A Scalable Dual-Polarized 256-Element Ku-Band Phased-Array SATCOM Receiver with ±70° Beam Scanning," in *2018 IEEE/MTT-S Int.l Microw. Symp.*, pp. 1203–1206, June 2018. ISSN: 2576-7216.

[9] A. Nafe, M. Sayginer, K. Kibaroglu, and G. M. Rebeiz, "2x 64-Element Dual-Polarized Dual-Beam Single-Aperture 28-GHz Phased Array With 2x 30 Gb/s Links for 5G Polarization MIMO," *IEEE Trans. Microw. Theory Techn.*, pp. 1–1, 2020.

[10] G. Oliveri, F. Caramanica, C. Fontanari, and A. Massa, "Rectangular Thinned Arrays Based on McFarland Difference Sets," *IEEE Trans. Antennas Propag.*, vol. 59, pp. 1546–1552, May 2011.

[11] D. Leeper, "Isophoric arrays-massively thinned phased arrays with well-controlled sidelobes," *IEEE Trans. Antennas Propag.*, vol. 47, pp. 1825–1835, Dec. 1999.

[12] P. Rocca, G. Oliveri, R. J. Mailloux, and A. Massa, "Unconventional Phased Array Architectures and Design Methodologies—A Review," *Proc. IEEE*, vol. 104, pp. 544–560, Mar. 2016.

[13] G. Oliveri, M. Carlin, and A. Massa, "Complex-Weight Sparse Linear Array Synthesis by Bayesian Compressive Sampling," *IEEE Trans. Antennas Propag.*, vol. 60, pp. 2309–2326, May 2012.

[14] Y. Lo and S. Lee, "A study of space-tapered arrays," *IEEE Trans. Antennas Propag.*, vol. 14, no. 1, pp. 22–30, 1966.

[15] G. Oliveri and A. Massa, "Bayesian compressive sampling for pattern synthesis with maximally sparse non-uniform linear arrays," *IEEE Trans. Antennas Propag.*, vol. 59, no. 2, pp. 467–481, 2011.

[16] G. Lockwood, P.-C. Li, M. O'Donnell, and F. Foster, "Optimizing the radiation pattern of sparse periodic linear arrays," *IEEE Trans. Ultrason. Ferroelectr. Freq. Control*, vol. 43, no. 1, pp. 7–14, 1996.

[17] A. K. Bolstad, J. D. Chisum, and J. E. Vian, "Methods and apparatus for array-based compressed sensing," U.S. Patent 10,367,674 B2, Jul. 2019.

[18] R. Mailloux, *Phased Array Antenna Handbook, Third Edition*. Artech House, 2017.

[19] N. C. Garcia and J. D. Chisum, "High-Efficiency, Wideband GRIN Lenses With Intrinsically Matched Unit Cells," *IEEE Trans. Antennas Propag.*, vol. 68, pp. 5965–5977, Aug. 2020.

[20] A. Papathanasopoulos, Y. Rahmat-Samii, N. C. Garcia, and J. D. Chisum, "A novel collapsible flat-layered metamaterial gradient-refractive-index lens antenna," *IEEE Trans. Antennas Propag.*, vol. 68, no. 3, pp. 1312–1321, 2020.

[21] E. Erfani, M. Niroo-Jazi, and S. Tatu, "A High-Gain Broadband Gradient Refractive Index Metasurface Lens Antenna," *IEEE Trans. Antennas Propag.*, vol. 64, pp. 1968–1973, May 2016.

[22] Y. Li, L. Ge, M. Chen, Z. Zhang, Z. Li, and J. Wang, "Multibeam 3-D-Printed Luneburg Lens Fed by Magnetoelectric Dipole Antennas for Millimeter-Wave MIMO Applications," *IEEE Trans. Antennas and Propag.*, vol. 67, pp. 2923–2933, May 2019.

[23] B. Soumitra and M. Mirotznik, "High gain, wide-angle QCTO-enabled modified Luneburg lens antenna with broadband anti-reflective layer," *Nature Sci. Rep.*, vol. 10, no. 1, 2020.

[24] Z. N. Chen, Y. Su, and W. E. I. Liu, "Metantennas: Flat Luneburg Lens Antennas Using Transformation Optics Method (TOM)," in *2020 Intl. Workshop Antenna Techn. (iWAT)*, pp. 1–3, Feb. 2020.

[25] Y. Su and Z. N. Chen, "A flat dual-polarized transformation-optics beamscanning luneburg lens antenna using pcb-stacked gradient index metamaterials," *IEEE Trans. Antennas Propag.*, vol. 66, pp. 5088–5097, Oct 2018.

[26] C. Wang, J. Wu, and Y.-X. Guo, "A 3-D-Printed Multibeam Dual Circularly Polarized Luneburg Lens Antenna Based on Quasi-Icosahedron Models for Ka-Band Wireless Applications," *IEEE Trans. Antennas Propag.*, vol. 68, pp. 5807–5815, Aug. 2020.

[27] W. Wang, N. Garcia, and J. Chisum, "The Systematic Design of Non-commensurate Impedance Matching Tapers for Ultra Wideband Gradient-Index (GRIN) Lens Antennas," *IEEE Trans. Antennas Propag.*, pp. 1–1, 2021.

[28] S. Zhang, R. K. Arya, W. G. Whittow, D. Cadman, R. Mittra, and J. Vardaxoglou, "Ultra-Wideband Flat Metamaterial GRIN Lenses Assisted with Additive Manufacturing Technique," *IEEE Trans. Antennas Propag.*, pp. 1–1, 2020.

[29] Y. He and G. V. Eleftheriades, "Matched, Low-Loss, and Wideband Graded-Index Flat Lenses for Millimeter-Wave Applications," *IEEE Trans. Antennas Propag.*, vol. 66, pp. 1114–1123, Mar. 2018.

[30] N. Garcia and J. Chisum, "Reduced dimensionality optimizer for efficient design of wideband millimeter-wave 3D metamaterial GRIN lenses," *Microw. Opt. Techn. Lett.*, vol. 63, no. 5, pp. 1372–1376, 2021.

[31] A. Petosa and A. Ittipiboon, "Design and performance of a perforated dielectric fresnel lens," *IEE Proc. - Microw., Antennas Propag.*, vol. 150, pp. 309–314, Oct. 2003.

[32] M. Imbert, A. Papió, F. D. Flaviis, L. Jofre, and J. Romeu, "Design and Performance Evaluation of a Dielectric Flat Lens Antenna for Millimeter-Wave Applications," *IEEE Antennas Wireless Propag. Lett.*, vol. 14, pp. 342–345, 2015.

[33] C. Mateo-Segura, A. Dyke, H. Dyke, S. Haq, and Y. Hao, "Flat luneburg lens via transformation optics for directive antenna applications," *IEEE Trans. Antennas Propag.*, vol. 62, pp. 1945–1953, April 2014.

[34] R. K. Luneburg and H. Mendlowitz, "Mathematical Theory of Optics," *Physics Today*, vol. 18, p. 63, 1965.

[35] N. Garcia, W. Wang, and J. Chisum, "Feed corrective lenslets for enhanced beamscan in flat lens antenna systems," vol. 30, no. 8, pp. 13047–13058. Publisher: Optica Publishing Group.

[36] N. Garcia and J. Chisum, "Compound grin fanbeam lens antenna with wideband wide-angle beam-scanning," *IEEE Trans. on Antennas and Propag.*, pp. 1–1, 2022.

[37] M. Cooley, "Phased array fed reflector (PAFR) antenna architectures for space-based sensors," in *2015 IEEE Aerospace Conference*, 2015.

[38] N. J. G. Fonseca, E. Girard, and H. Legay, "Hybrid array fed reflector antenna solution for broadband satellite communications," in *2017 11th European Conf. Antennas Propag. (EUCAP)*, pp. 2645–2648, 2017.

[39] A. Dubok, A. Al-Rawi, G. Gerini, and A. B. Smolders, "Reflector synthesis for wide-scanning focal plane arrays," *IEEE Trans. Antennas Propag.*, vol. 67, no. 4, pp. 2305–2319, 2019.

[40] A. van den Biggelaar, A. Al-Rawi, U. Johannsen, and A. Smolders, "64 element active phased array as focal plane array feed for reflector antennas for mm-wave wireless communications," in *2020 14th European Conf. Antennas Propag. (EuCAP)*, pp. 1–5, 2020.

[41] Z. Qu, S.-W. Qu, Z. Zhang, S. Yang, and C. H. Chan, "Wide-Angle Scanning Lens Fed by Small-Scale Antenna Array for 5G in Millimeter-Wave Band," *IEEE Trans. Antennas Propag.*, vol. 68, pp. 3635–3643, May 2020.

[42] A. Artemenko, A. Mozharovskiy, S. Tikhonov, A. Myskov, and R. Maslennikov, "Multiple-feed integrated lens antenna with continuous scanning range," in *2017 11th European Conf. Antennas Propag. (EUCAP)*, pp. 2795–2799, Mar. 2017.

© 2023 IEEE. Personal use is permitted, but republication/redistribution requires IEEE permission. See https://www.ieee.org/publications/rights/index.html for more information.
Authorized licensed use limited to: UNIVERSITY NOTRE DAME. Downloaded on February 14,2023 at 18:29:53 UTC from IEEE Xplore. Restrictions apply.

This article has been accepted for publication in IEEE Transactions on Antennas and Propagation. This is the author's version which has not been fully edited and content may change prior to final publication. Citation information: DOI 10.1109/TAP.2023.3240085

[43] P.-Y. Feng, S.-W. Qu, S. Yang, L. Shen, and J. Zhao, "Ku-Band Transmitarrays With Improved Feed Mechanism," *IEEE Trans. Antennas Propag.*, vol. 66, pp. 2883–2891, June 2018.

[44] N. T. Nguyen, R. Sauleau, M. Ettorre, and L. Le Coq, "Focal Array Fed Dielectric Lenses: An Attractive Solution for Beam Reconfiguration at Millimeter Waves," *IEEE Trans. Antennas Propag.*, vol. 59, pp. 2152–2159, June 2011.

[45] Z. Wang, Y. Song, S. Fan, and Y. Fan, "A Scanning Angle Adjustment Method for Array-Fed Lens Antenna Systems," *IEEE Antennas Wireless Propag. Lett.*, vol. 20, pp. 868–872, May 2021.

[46] Y. Zeng and R. Zhang, "Millimeter wave mimo with lens antenna array: A new path division multiplexing paradigm," *IEEE Transactions on Communications*, vol. 64, no. 4, pp. 1557–1571, 2016.

[47] Y. Zeng and R. Zhang, "Cost-effective millimeter-wave communications with lens antenna array," *IEEE Wireless Commun.*, vol. 24, no. 4, pp. 81–87, 2017.

[48] S. Blank and W. Imbriale, "Array feed synthesis for correction of reflector distortion and vernier beamsteering," *IEEE Trans. Antennas Propag.*, vol. 36, p. 1351–1358, Oct 1988.

[49] B. Saka and E. Yazgan, "Pattern optimization of a reflector antenna with planar-array feeds and cluster feeds," *IEEE Trans. Antennas Propag.*, vol. 45, p. 93–97, Jan 1997.

[50] C. T. Sletten, *Reflector and Lens Antennas*. John Wiley Sons, 1988.

[51] S. K. Karki, M. Varonen, M. Kaunisto, A. Rantala, M. Lahti, A. Lamminen, J. Holmberg, M. Kantanen, J. Ala-Laurinaho, and V. Viikari, "Beam-reconfigurable antenna based on vector modulator and rotman lens on ltcc," *IEEE Access*, vol. 9, pp. 52872–52882, 2021.

[52] M. Chen, D. Wang, Z. Wang, and W. Wang, "A continuous-time algorithm with the sigmoid function for distributed constrained optimization of multi-agent systems," in *2020 7th International Conference on Information, Cybernetics, and Computational Social Systems (ICCSS)*, pp. 687–692, 2020.

[53] M. Ruppert, V. Bertsch, and W. Fichtner, "Optimal load shedding in distributed networks with sigmoid cost functions," in *2015 International Symposium on Smart Electric Distribution Systems and Technologies (EDST)*, pp. 159–164, 2015.

[54] W. Liu, Z. Wang, Y. Yuan, N. Zeng, K. Hone, and X. Liu, "A novel sigmoid-function-based adaptive weighted particle swarm optimizer," *IEEE Trans. Cybern*, vol. 51, no. 2, pp. 1085–1093, 2021.

[55] "IEEE draft recommended practice for near-field antenna measurements," *IEEE P1720/D2, April 2012*, pp. 1–105, 2012.

[56] M. Giordani, M. Mezzavilla, and M. Zorzi, "Initial Access in 5G mmWave Cellular Networks," *IEEE Commun. Mag.*, vol. 54, pp. 40–47, Nov. 2016.

[57] J. Budhu and Y. Rahmat-Samii, "A novel and systematic approach to inhomogeneous dielectric lens design based on curved ray geometrical optics and particle swarm optimization," *IEEE Trans. on Antennas and Propag.*, vol. 67, no. 6, pp. 3657–3669, 2019.

[58] W. Wang and J. Chisum, "Hybrid geometrical optics and uniform asymptotic physical optics for rapid and accurate practical grin lens design," in *2022 IEEE MTT-S Int. Microw. Symp. Dig.*, pp. 20–23, 2022.

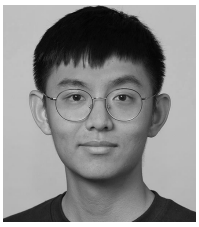

Wei Wang is pursuing a Ph.D in Electrical Engineering at the University of Notre Dame in Indiana, U.S.A. In 2019, he received the B.S. degree in electrical engineering from Nankai University in Tianjin, China. His research interests are gradient index(GRIN) lens antennas design and computational electromagnetics for GRIN lenses.

Nicholas Estes received the B.S. degree in electrical engineering from the University of Oklahoma in 2016. He is currently pursuing a Ph.D. at the University of Notre Dame, where his research interests include microwave lens antennas, low-resolution low-power mmW transceceivers, nonlinear circuits, and their applications in energy-efficient next-generation wireless systems.

Nicolas C. Garcia received the Ph.D. degree in electrical engineering from the University of Notre Dame in 2022. He is the founder and CEO of Cheshir Industries, Inc., which develops low-profile gradient index (GRIN) lens technology for emerging 5G and millimeter wave applications.

Matthew Roddy received the B.S. degree in electrical engineering and physics from the University of Notre Dame in 2021. He is now pursuing a Ph.D. in Physics at Cornell University. His research interests are in condensed matter, particularly growing and investigating novel quantum materials.

Andrew K. Bolstad (S'03–M'09–SM'15) was born in Madison, WI, USA. He received the B.S. degree (with distinction) from Iowa State University, Ames, IA, USA, and the M.S. and Ph.D. degrees from the University of Wisconsin, Madison, WI, USA, all in electrical engineering.

He is currently an Adjunct Assistant Professor with Iowa State University. From 2009 to 2017, he held the position of Technical Staff with MIT Lincoln Laboratory. His research interests include nonlinear digital compensation, RF fingerprinting, sparse models, compressed sensing, data science, and machine learning.

Dr. Bolstad is a senior member of the IEEE and a member of the Signal Processing Society. He has co-authored over twenty journal and conference papers and has been awarded five patents. He has won several teaching awards, was a co-author of the 2015 GOMACTech Best Poster Paper, and was a recipient of the 2012 MIT Lincoln Laboratory Team Award.

Jonathan D. Chisum (S'02–M'06–SM'17) received the Ph.D. in Electrical Engineering from the University of Colorado at Boulder in Boulder, Colorado USA, in 2011. He is currently an Associate Professor of Electrical Engineering at the University of Notre Dame.

From 2012 to 2015 he was a Member of Technical Staff at the Massachusetts Institute of Technology Lincoln Laboratory in the Wideband Communications and Spectrum Operations groups. His work at Lincoln Laboratory focused on millimeter-wave phased arrays, antennas, and transceiver design for electronic warfare applications. In 2015 he joined the faculty of the University of Notre Dame. His research interests include millimeter-wave communications and spectrum sensing using novel and engineered materials and devices to dramatically lower the power and cost and enable pervasive deployments. His group focuses on gradient index (GRIN) lenses for low-power millimeter-wave beam-steering antennas, nonlinear (1-bit) radio architectures for highly efficient communications and sensing up through millimeter-waves, phase-change materials for reconfigurable RF circuits for wideband distributed circuits and antennas, and microwave/spin-wave structures for low-power and chip-scale analog signal processing for spectrum sensing and protection.

Dr. Chisum is a senior member of the IEEE, a member of the American Physical Society, and an elected Member of the U.S. National Committee (USNC) of the International Union or Radio Science's (URSI) Commission D (electronics and photonics). He is the current Chair for USNC URSI Commission D: Electronics and Photonics. He is also an Associate Editor for IET Electronics Letters.

© 2023 IEEE. Personal use is permitted, but republication/redistribution requires IEEE permission. See https://www.ieee.org/publications/rights/index.html for more information.
Authorized licensed use limited to: UNIVERSITY NOTRE DAME. Downloaded on February 14,2023 at 18:29:53 UTC from IEEE Xplore. Restrictions apply.